

General Disclaimer

One or more of the Following Statements may affect this Document

- This document has been reproduced from the best copy furnished by the organizational source. It is being released in the interest of making available as much information as possible.
- This document may contain data, which exceeds the sheet parameters. It was furnished in this condition by the organizational source and is the best copy available.
- This document may contain tone-on-tone or color graphs, charts and/or pictures, which have been reproduced in black and white.
- This document is paginated as submitted by the original source.
- Portions of this document are not fully legible due to the historical nature of some of the material. However, it is the best reproduction available from the original submission.

ERT

NASA

Document No. P-1143F
Type III Report
February, 1977

Prepared for
Goddard Space Flight Center
Greenbelt, Maryland 20771

Estimation of the geophysical properties of the ocean surface using aircraft microwave measurements

(NASA-CF-152479) ESTIMATION OF THE
GEOPHYSICAL PROPERTIES OF THE OCEAN SURFACE
USING AIRCRAFT MICROWAVE MEASUREMENTS Final
Report, Aug. 1974 - Aug. 1976 (Environmental
Research and Technology, Inc.) 66 p HC

N77-21817

HC AD4/MF AD1

Unclass

G3/48 24442

Prepared by
Mary Grace Fowler
James H. Willand
David T. Chang
Ronald G. Isaacs



Prepared for
Goddard Space Flight Center
Greenbelt, Maryland 20771

Estimation of the geophysical properties of the ocean surface using aircraft microwave measurements

Prepared by
Mary Grace Fowler
James H. Willand
David T. Chang
Ronald G. Isaacs

1. Report No.		2. Government Accession No.		3. Recipient's Catalog No.	
4. Title and Subtitle Estimation of the Geophysical Properties of the Ocean Surface Using Aircraft Microwave Measurements				5. Report Date February, 1977	
				6. Performing Organization Code	
7. Author(s) Mary Grace Fowler David T. Chang James H. Willand Ronald G. Isaacs				8. Performing Organization Report No. P1143F	
9. Performing Organization Name and Address Environmental Research & Technology Inc. 696 Virginia Road Concord, Massachusetts				10. Work Unit No.	
				11. Contract or Grant No. NAS5-20619	
12. Sponsoring Agency Name and Address NASA Goddard Space Flight Center Greenbelt, Maryland 20771				13. Type of Report and Period Covered Final Report August 1974-August 1976	
				14. Sponsoring Agency Code	
15. Supplementary Notes Technical Monitor: Dr. Per Gloersen, Code 901					
16. Abstract An improved model of the effects of sea state on microwave signature has been developed which incorporates the different effects of whitecaps and streaks to define the response of microwave channels to wind speed. This model has been demonstrated to agree with recent measurements. An approximation model has also been incorporated to describe the effects of precipitation on microwave radiation through a computationally rapid routine. The use of these models and a new technique to allow the selection of the most climatologically appropriate D-Matrix is demonstrated in the inversion of data collected by the NASA CV-990 over the Bering Sea. Surface wind speed agrees very well with observations while good results are obtained for integrated water vapor, and liquid water.					
17. Key Words (Suggested by Author(s)) microwave simulation microwave inversion sea surface roughness precipitation modeling				18. Distribution Statement Unclassified - Unlimited	
19. Security Classif. (of this report)		20. Security Classif. (of this page)		21. No. of Pages	
				22. Price*	

TABLE OF CONTENTS

	Page
LIST OF ILLUSTRATIONS	v
LIST OF TABLES	vii
1. INTRODUCTION	1
1.1 Objective	1
1.2 Summary of Results	2
2. IMPROVEMENTS OF PHYSICAL MODELS	3
2.1 The Sea Surface Roughness Model	3
2.1.1 Observations	3
2.1.2 Radiative Properties of Foam Components	10
2.1.3 The Foam Model	12
2.1.4 Model Evaluation	15
2.2 Precipitation Model	18
2.2.1 Background	18
2.2.2 Theoretical Considerations of the Extinction Model	20
2.2.3 Approximations of the Extinction Model	21
2.2.4 The Precipitation Drop Size Model	25
2.2.5 The Combined Model	27
3. INVERSION PROCEDURE OPTIMIZATION	29
3.1 Summary of the Inversion Procedure	29
3.2 D-Matrix Selection	31
3.3 Nonlinearities	34
3.4 Channel-Parameter Correlations	36
4. INVERSION OF BESEX DATA	43
4.1 The BESEX Equipment	43
4.2 Meteorological Conditions for 3 March 1973	43
4.3 Microwave Measurements	49
4.4 Inversion Results	49
5. CONCLUSIONS AND RECOMMENDATIONS	57
6. REFERENCES	59

LIST OF ILLUSTRATIONS

Figure		Page
2-1	Empirical Relationship Between Change in Brightness Temperature and Wind Speed	4
2-2	Calculated and Observed Dependence of Differential Brightness Temperature on Foam Cover	5
2-3	Comparison of Observations of Wind Speed vs Percent Foam Cover	7
2-4	Wind and Sea Scale for a Fully Developed Sea	9
2-5	Calculated Relationship Between Change in Brightness Temperature and Foam Cover	13
2-6	Calculated Relationship Between Change in Brightness Temperature and Wind Speed	14
2-7	Computed Change in Brightness Temperature Using Three Foam Models	16
2-8	Microwave Channel Response to Wind Speed	17
2-9	Comparison of Change in Brightness Temperature Due to Increase with Wind Speed	19
2-10	Range of Drop Sizes and Mie Efficiency Factors for Full Mie Theory and Linear Segment Approximation	23
3-1	Flow Diagram for Application of the Data Inversion Methodology to Parameter Estimation for a Radiometric Experiment	30
3-2	Brightness Temperature Differences vs Cloud Liquid Water Content	35
3-3	Correlation Coefficients Between Microwave Measurements and Sea Surface Temperature	39
3-4	Correlation Coefficients Between Microwave Measurements and Surface Wind Speed	40
3-5	Correlation Coefficients Between Microwave Measurements and Atmospheric Water Vapor and Liquid Water	41
4-1	Surface Chart for the BESEX Area, 0000 GMT, March 3, 1973	44
4-2	Air Masses along the CV-990 Flight Track	46

PRECEDING PAGE BLANK NOT FILMED.

LIST OF ILLUSTRATIONS

Figure		Page
4-3	Clouds, Temperatures and Winds along the CV-990 Flight Track	47
4-4	Microwave Measurements from 11 km, 3 March 1973	50
4-5	Multi Channel Microwave Field of View for 11 km	51
4-6	Inversion Results from the Measurements Made in the 11 km Data Set Run	54

LIST OF TABLES

Table		Page
3-1	Microwave Channels and Geophysical Parameters Used in the Inversion Analysis	32
3-2	Inversion Results - 60 Observations for <u>D</u> and 60 Observations for Evaluation	33
3-3	Clear - No Noise - D-Matrix	42
3-4	Cloudy - No Noise - D-Matrix	43
4-1	Microwave Radiometer Offsets and System Noise	52

1. INTRODUCTION

1.1 Objective

A number of techniques have been developed to infer geophysical parameters from remote sensing measurements. One such technique is the statistical estimation of parameters described by Gaut et al. (1972) and Willand et al. (1973). This technique has been implemented at the Goddard Space Flight Center (GSFC) to operate on microwave remote sensing measurements obtained on aircraft flight programs. The objective of the present study is to improve the routines implemented at GSFC for statistical estimation of parameters.

The basic elements of the inversion procedure at GSFC are:

- routines to simulate physical parameters of the geophysical system and the associated brightness temperatures as measured by a remote sensor;
- routines to form the statistical relationship between the geophysical parameters and the simulated brightness temperatures;
- routines to apply the a priori statistical relationship to actual measured brightness temperature to infer the corresponding geophysical parameters.

In the present study, the following tasks were performed:

- Development of an improved sea surface roughness model;
- Extension of the cloud model to simulate better the radiometric properties of precipitation;
- Investigation of the effects of the inclusion of non-linear terms in the correlation matrices;
- Investigation of the effects of decision-making procedures in the operational application of the inversion method.

These new models and procedures were applied to a data sample selected from the CV-990 flights for test and evaluation.

1.2 Summary of Results

The surface roughness model of Stogryn (1967) and others are extended to include the specification of the effects of foam as a function of wind speed. The model results are compared to recent measurements obtained during the Bering Sea Experiment (BESEX) by instrumentation on the CV-990 aircraft. Computation of the change in brightness temperature with wind speed agreed well with the measured data.

Effects of large droplets were approximated by extending the Staelin approximation (Staelin, 1966) to include higher order terms of the Mie expansion with the condition that the total expression for extinction be solvable in closed form. The drop size distribution for rain used in this model was basically that described by Marshall and Palmer (1948).

The effects of non-linearities and real-time decision making on the accuracy of inversion results were investigated by application to a sample of BESEX data which included both cloudy and clear-sky cases. These results show that the inclusion of the non-linear terms selected in the study in the D-matrix does not appear to alter the inversion results significantly. On the other hand, the use of the proper D-matrix does improve the inversion results, at least in the statistical sense.

In this report, the improved physical models of sea state and precipitation effects on microwave radiation will be discussed in Section 2. Section 3 will present the techniques used to extend the inversion procedures, while Section 4 will apply these techniques to the inversion of aircraft data during BESEX. The conclusions and recommendations will be summarized in Section 5, while complete listings and discussions of the routines implemented on the Goddard computer system will appear in the Appendix.

2. IMPROVEMENTS OF PHYSICAL MODELS

Two physical models were improved -- those of sea surface roughness and precipitation. The characteristics of the improved models are described in this section.

2.1 The Sea Surface Roughness Model

2.1.1 Observations

The microwave radiative properties of the ocean surface determine both the surface-emitted thermal radiation and the surface-reflected component of the downwelling atmospheric radiation. Observations have indicated that the surface properties are characterized by the general "sea state" manifested in: (a) the spatial and spectral distribution of elemental sea slopes; and (b) the percentage of the surface covered by various forms of white water or foam. The effects of the former factor on observed brightness temperature are presently incorporated within the ocean surface submodel.

Subsequent observations aimed at isolating the role played by ocean foam indicate that it may be the more significant determinant of the brightness temperature. Figure 2-1 (from Nordberg et al., 1971) demonstrates, empirically, the relationship between change in brightness temperature (relative to a calm, foam-free sea) and wind speed. These observations yield a wind speed (U) vs. differential brightness temperature (ΔT_B) relationship of:

$$\begin{aligned} \Delta T_B \text{ (K)} &= 1.29 U \text{ (m sec}^{-1}\text{)} - 10.3 & U \geq 8 \text{ m sec}^{-1} \\ &= 0 & U < 8 \text{ m sec}^{-1} \end{aligned} \quad (2-1)$$

However, the surface models previously implemented at the GSFC calculate brightness temperature (and hence ΔT_B) based on the foam coverage surface percentage and not by relating ΔT_B and U empirically. Therefore an intermediate relationship of the surface foam cover dependence on wind speed is needed. The white cap model of Cardone (1969) provides a semi-empirical theoretical approach to obtain such a relationship. Figure 2-2

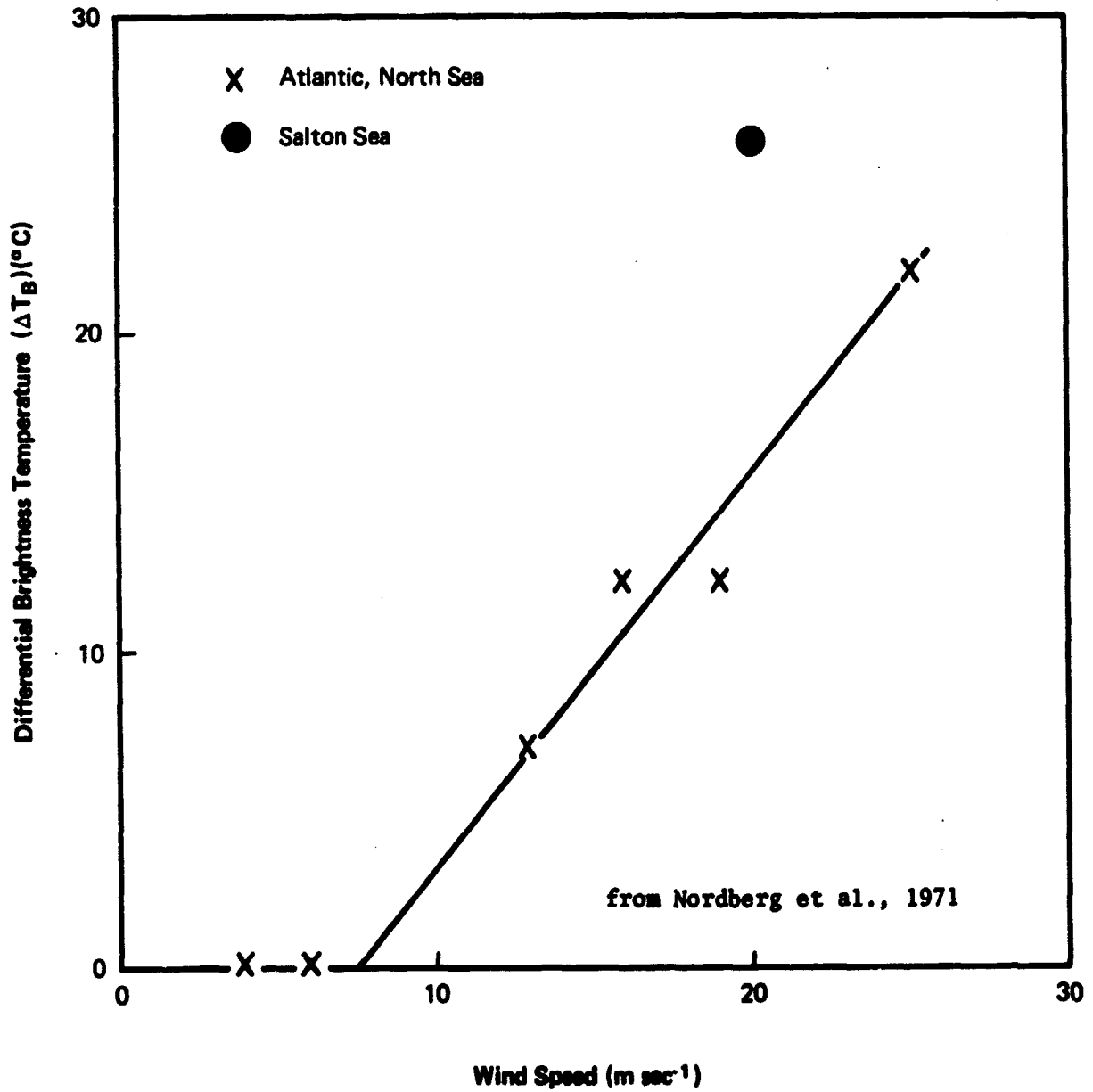


Figure 2-1 Empirical Relationship Between Change in Brightness Temperature and Wind Speed

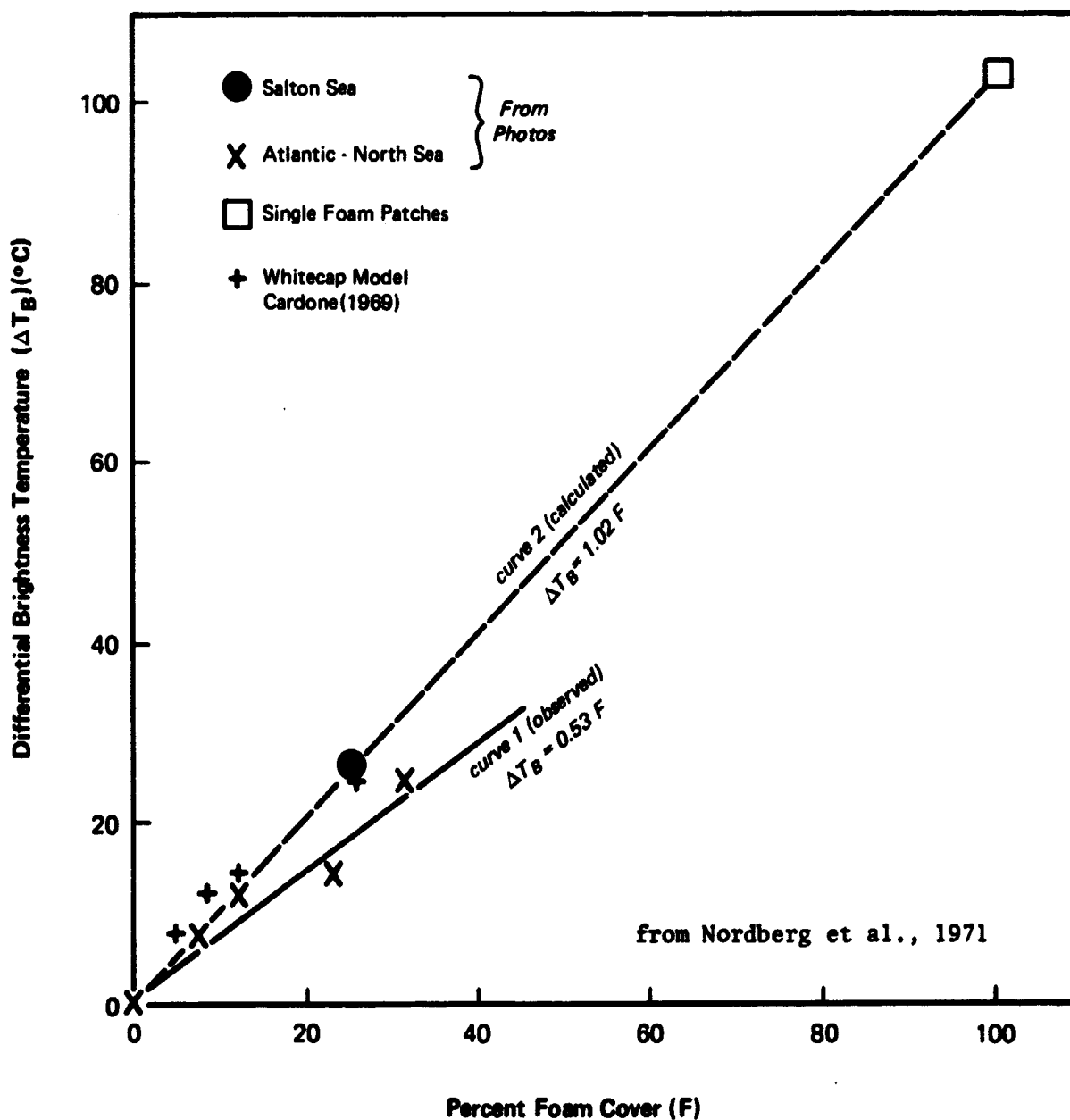


Figure 2-2 Calculated and Observed Dependence of Differential Brightness Temperature on Foam Cover

illustrates the dependence of differential brightness temperature on foam cover based on: (a) observations - curve 1 and (b) Cardone's model - curve 2 which is fitted by the line:

$$F \text{ (percent foam cover)} = 1.26 U \text{ (m sec}^{-1}\text{)} - 10.1 \quad (2-2)$$

Equation (2-2) was previously used to predict surface foam cover. Note that there appears to be a discrepancy between observed and theoretical foam vs. wind speed (and hence differential brightness temperature vs. foam cover) results. In this study, an attempt has been made, based on subsequent work by Ross and Cardone (1974), to resolve observation and theory and arrive at a self-consistent surface model. In this approach, the dependence of foam cover vs. wind speed has been considered independently of the radiative properties of the foam.

Figure 2-3 plots observations of wind speed vs. percent foam cover from three observers. The fractions of white cap are plotted separately from those of total foam, consisting of both white caps and streaks. Streaks consist of broken white caps caught by the surface wind and drawn across the surface in the wind direction. White caps are generally isotropically distributed within an area element while streaks will generally be oriented in the direction of the surface wind field. In reconciling curves 1 and 2 in Figure 2-2, two possibilities exist. Either observations from photographs overestimate foam cover, or the theoretical curves underestimate total foam (Nordberg, et al., 1971).

Ross and Cardone (1974) emphasize that the effect of streaks was neglected in Cardone's earlier formulation. Therefore, the previously implemented relationship of foam cover versus wind speed must be amended. In Webster et al. (1974), it is remarked that even unit emissivity for the observed white caps cannot account for the increase in brightness temperature and that the radiometrically significant part of the foam fraction must be the streaks. As can be seen in Figure 2-3 there is a considerable amount of scatter in the data. (Note: the data from Webster et al. (1974) represents a 5-minute average of measurements over a fully developed sea.) The dotted line corresponds to Cardone's (1969) white cap model fitted by the polynomial expression:

$$F_w = -0.00188 U + 0.000263 U^2 - 0.00000295 U^3 + 0.00000085 U^4 \quad (2-3)$$

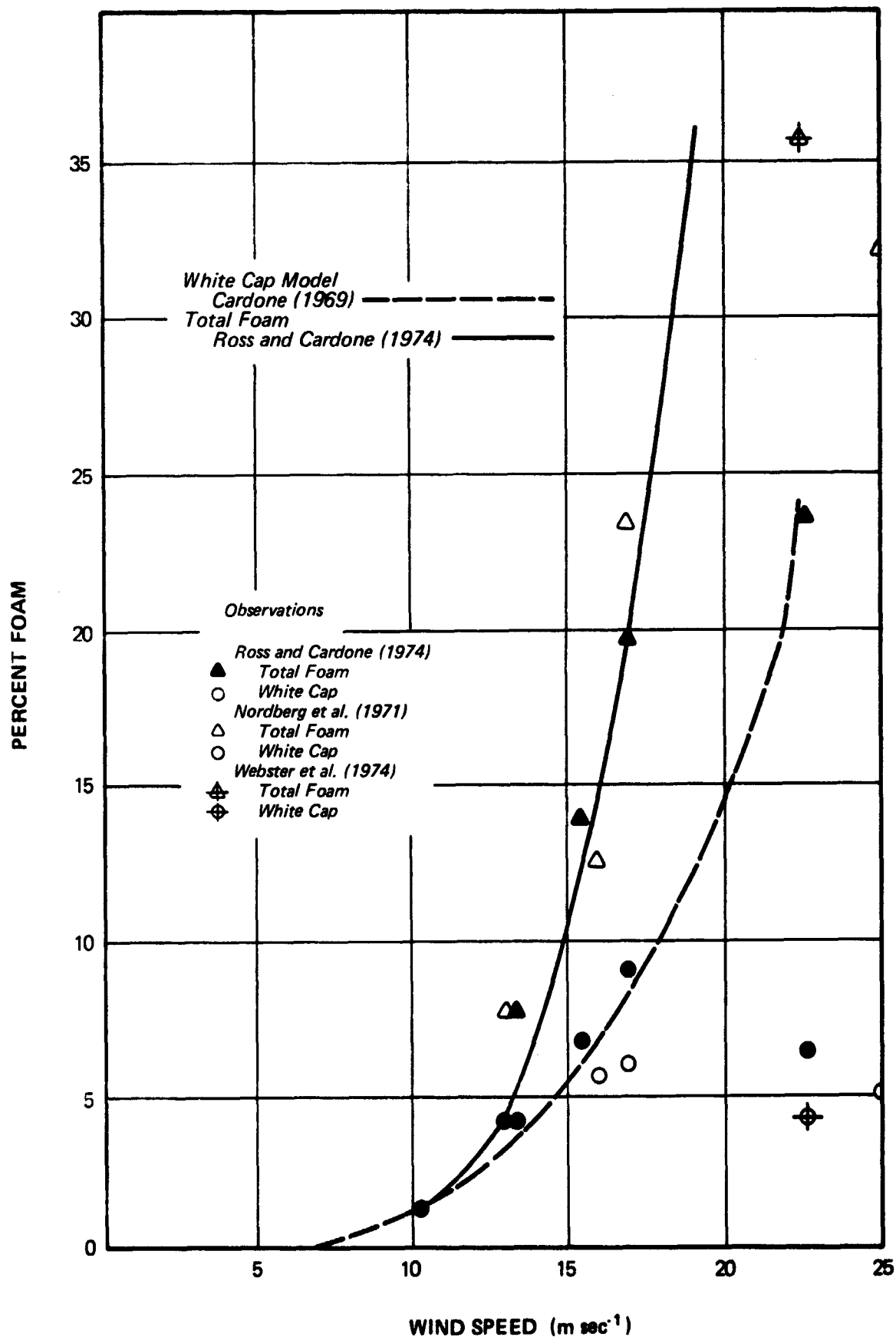


Figure 2-3 Comparison of Observations of Wind Speed vs Percent Foam Cover

The solid curve is a fit to Ross and Cardone's (1974) data for total foam (white cap and streaks) generated using the empirically derived relationship:

$$F_T = (1 + R_{sw}) F_w \quad (2-4)$$

where

F_T is the total percentage of foam cover

F_w is the percentage of white cap cover given by Cardone (Equation 2-3)

R_{sw} is the ratio of the percentage of streaks to the percentage of white caps:

$$= 0.255 U (\text{m sec}^{-1})^{-2.99}$$

Note that both total foam and white cap models fit observations relatively well in the region $U \leq 17 \text{ m sec}^{-1}$.

Ross and Cardone point out that the percentage cover observations for wind speed $U \geq 17 \text{ m sec}^{-1}$ lie considerably below what would be expected, based on theory, for fully developed sea conditions. In Figure 2-3 it can be seen that none of the chosen observations conform to theory within this high wind speed region. It is suggested that these represent cases where the sea is not fully developed due to limited fetch or duration. Figure 2-4, adapted from Stogryn (1967), gives the minimum fetch and duration for fully developed seas at a given wind speed. It is unlikely that sufficient duration and fetch is achieved at higher wind speeds for fully developed seas due to the extreme fetch and duration requirements. Therefore, foam cover, and particularly the fraction of streaks, may be overestimated at higher wind speeds (approximately 20 m sec^{-1}) if seas are not fully developed. Additionally, as a consequence of equations (2-3) and (2-4), the foam model saturates at approximately 22.3 m sec^{-1} , at which point there is 100 percent white water coverage.

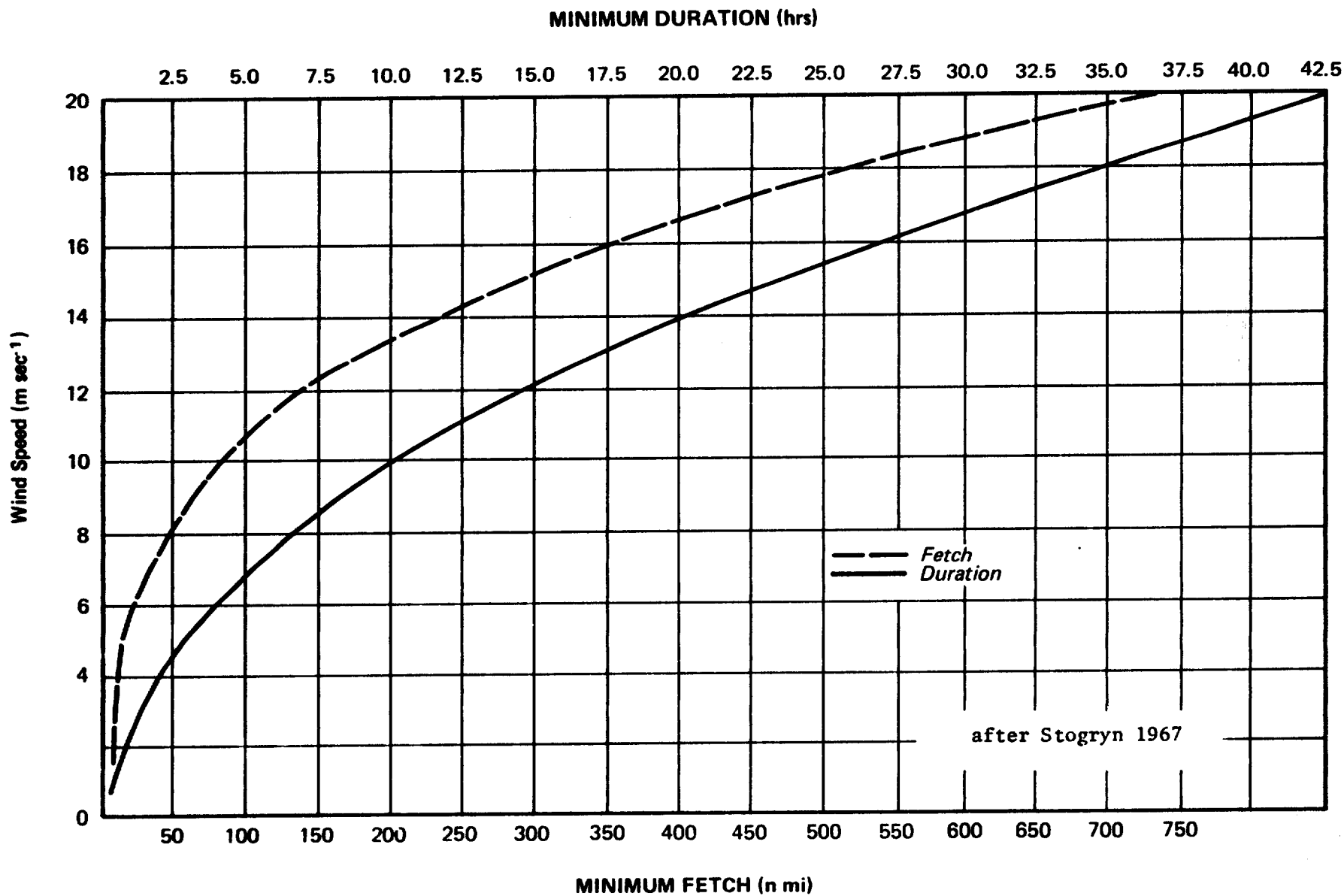


Figure 2-4 Wind and Sea Scale for a Fully Developed Sea

2.1.2 Radiative Properties of Foam Components

Both area coverage and radiative properties of a given foam component are necessary to predict radiometric results. These properties of sea foam may be computed given a viable physical model. The porous dielectric foam model of Rosenkranz (1971) has previously (for example, see Willand et al., 1974) been used to compute the absorption coefficient of a foam layer of given precipitable water content,

$$F = \rho QD = 0.004 \text{ g m}^{-2}$$

where

ρ is the density of the water

D is the depth of the foam layer

Q is the ratio of the volume of water in the foam to the total volume

There is no a priori reason for assuming that various foam components such as white caps and streaks have the same radiative properties. On the contrary, recent observational implications suggest that streaks are less emissive than white caps. Nordberg et al., (1971) suggests this explanation to reconcile the fit of curve 1 in Figure 2-1 with their data. Ross and Cardone (1974) in formulating a relationship between differential brightness temperature and foam cover as:

$$\Delta T_B = K_w F_w + K_s F_s \quad (2-6)$$

where

F_w is the percentage coverage of white caps

F_s is the percentage coverage of streaks

found that the ratio of coefficients K_s/K_w which fits their data is approximately 0.5. This concurs with the previous observations that streaks are less emissive. The discussion can be roughly quantified based on the following simple calculation:

The surface brightness temperature with white cap fraction f_w and streak fraction f_s is:

$$T_B(f_w, f_s) = f_s \left[\epsilon_s T_s + (1 - \epsilon_s) T_{sky} \right] + \left[f_w \epsilon_w T_s + (1 - \epsilon_w) T_{sky} \right] + (1 - f_s - f_w) \left[\epsilon_0 T_s + (1 - \epsilon_0) T_{sky} \right] \quad (2-7)$$

where

ϵ_s = streak emissivity

ϵ_w = white cap emissivity

ϵ_0 = foam-free rough surface emissivity

T_s = surface thermometric temperature

T_{sky} = black body sky temperature

f_s = $F_s/100$

f_w = $F_w/100$

The change in brightness temperature over a foam-free rough sea is then:

$$\begin{aligned} \Delta T_B &= T_B(f_w, f_s) - T_B(0,0) \\ &= (\epsilon_w - \epsilon_0) f_w + (\epsilon_s - \epsilon_0) f_s (T_s - T_{sky}) \end{aligned} \quad (2-8)$$

Comparing this expression with (2-6) requires that:

$$\frac{K_s}{K_w} \approx 0.5 = \frac{(T_s - T_{sky}) (\epsilon_s - \epsilon_0)}{(T_s - T_{sky}) (\epsilon_w - \epsilon_0)} \quad (2-9)$$

Assuming $\epsilon_0 = 0.4$ for the foam free surface and using $\epsilon_w - \epsilon_0 = 0.35$ [Rosenkranz (1971)] yields a streak emissivity of:

$$\epsilon_s \approx 0.58$$

or an approximate 25% decrease in streak emissivity as compared to white caps. Differential brightness temperature calculations based on Equations

2-3, 2-4 and 2-8 and the emissivities given above (assuming $(T_s - T_{sky}) \approx 273K$) are plotted in Figures 2-5 and 2-6 as functions of foam cover and wind speed, respectively. Agreement with observed values is remarkably good.

The emissivity difference between streak and white cap can be interpreted either in terms of intrinsic or geometrical properties; that is, the differing optical depths may be due to differing absorption coefficients or differing physical depths. Assuming (for lack of contradictory evidence) that the porous foam model describes both white caps and streaks, and given a constant foam mixing ratio, the indicated emissivity difference can correspond only to a change in characteristic depths between white cap and streak [Rosenkranz and Staelin (1972)]. This is consistent with observations and a suggestion by Webster et al. (1974).

The following calculation suggests the order of magnitude of the depth difference. Assume that for a surface layer

$$\epsilon_i = 1 - R_i = 1 - \exp(-2 \gamma_i d_i); (i = s, w) \quad (2-10)$$

where

ϵ_i = ith component emissivity

R_i = ith component reflectivity

γ_i = ith component absorption coefficient

d_i = ith component characteristic depth

Solving for the ratio of characteristic depths and assuming $\gamma_s = \gamma_w$ yields:

$$d_s/d_w \approx 0.6 \quad (2-11)$$

This order of magnitude (10^{-1}) is consistent with observations.

2.1.3 The Foam Model

Based on the above discussion and development, the new foam model may be summarized by the following set of equations:

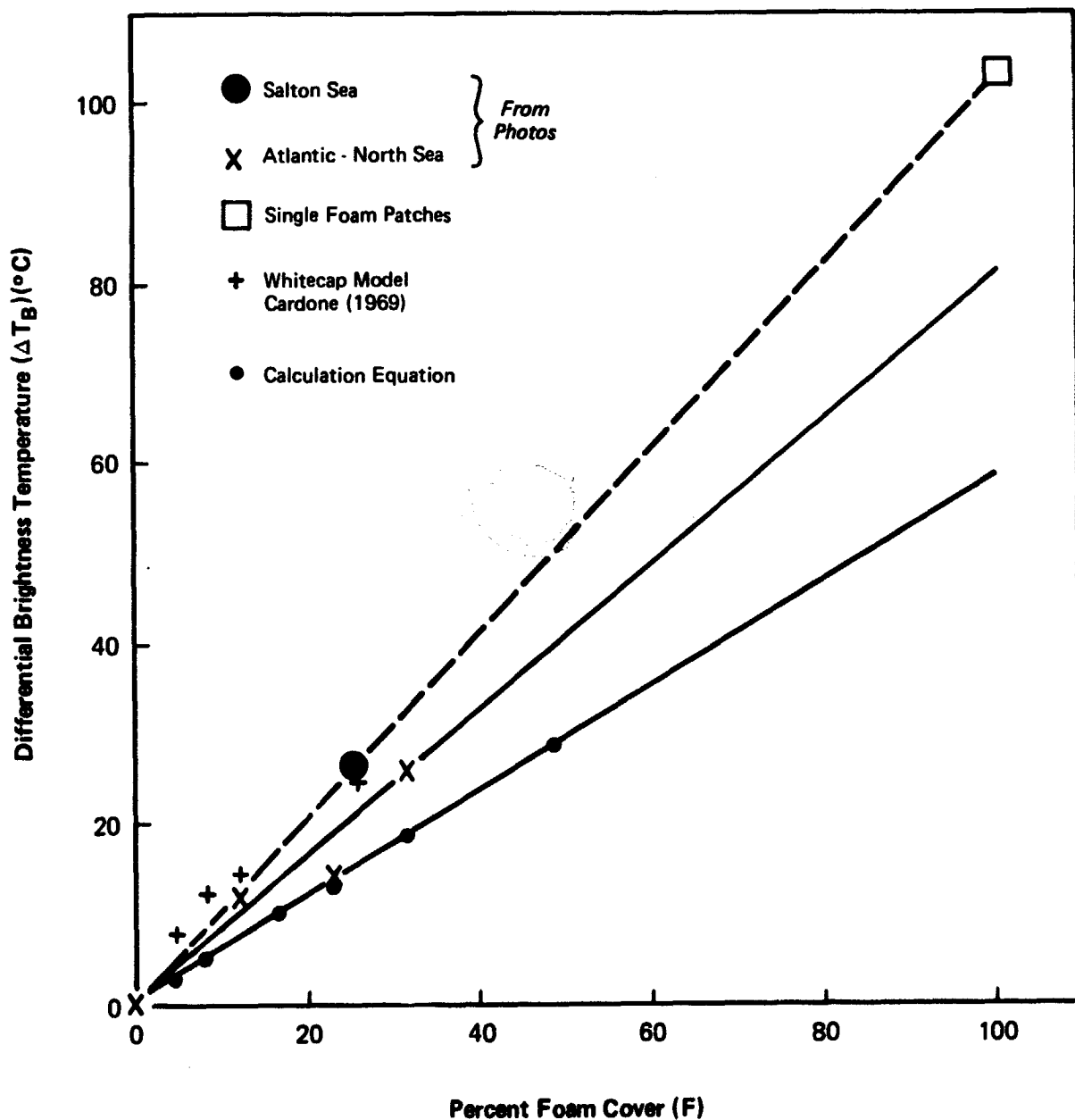


Figure 2-5 Calculated Relationship Between Change in Brightness Temperature and Foam Cover

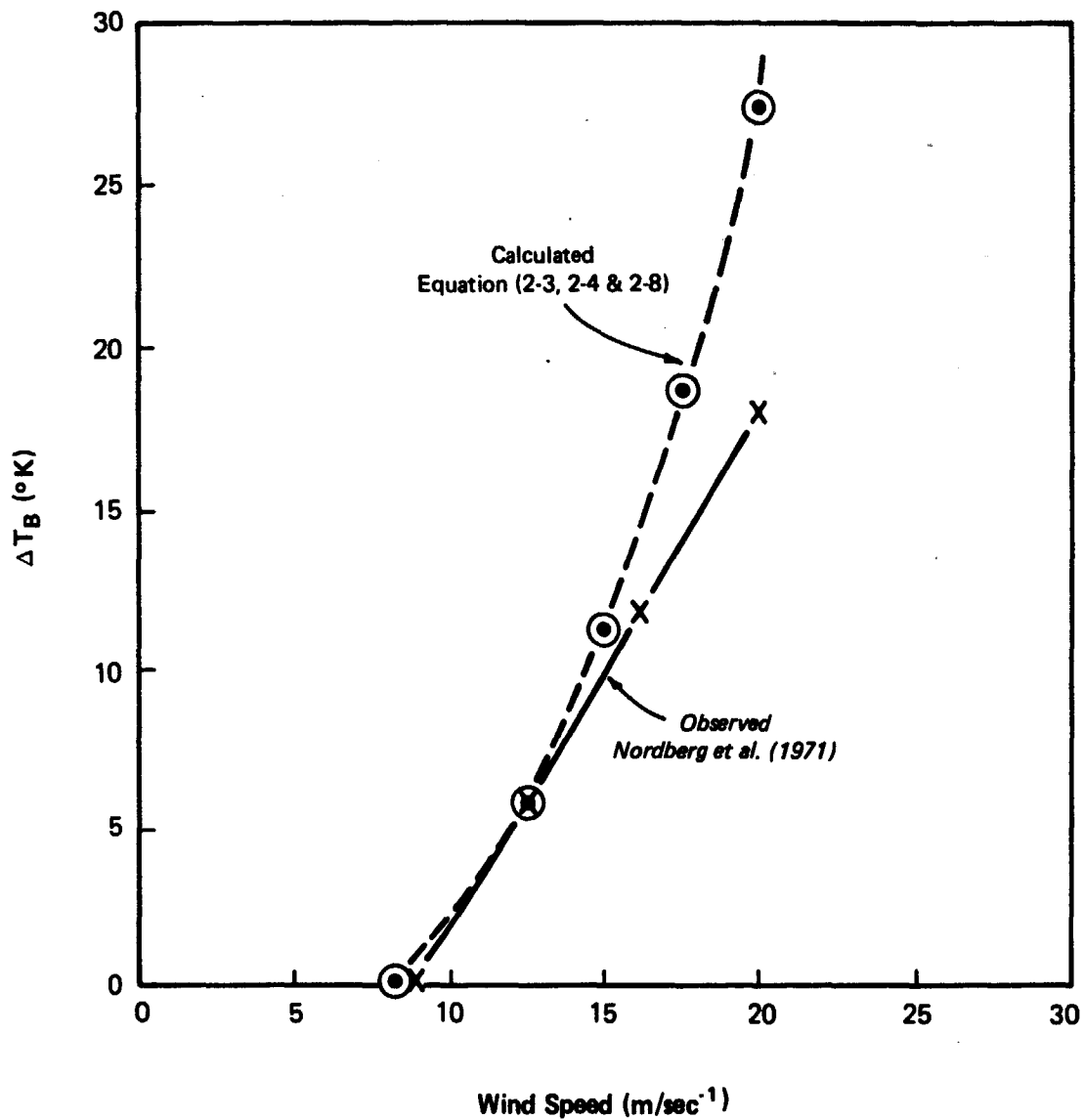


Figure 2-6 Calculated Relationship Between Change in Brightness Temperature and Wind Speed

$$F_w = -0.00188U + 0.000263U^2 - 0.00000295U^3 + 0.00000085U^4$$

$$F_s = (0.255U - 2.99) F_w$$

$$\gamma = 4\pi QK'' (\lambda, T, S)/3\lambda$$

$$\tau_i = \gamma d_i \quad (i = s, w)$$

$$TF = F_w \exp(-2d_w \gamma) + F_s \exp(-2d_s \gamma) + (1 - F_w - F_s)$$

where

F_w is surface white cap coverage

U is the resultant wind speed

F_s is surface streak coverage

γ is the attenuation coefficient of foam

Q is the foam mixing ratio

λ is the wavelength

T and S are respectively the temperature and salinity of the water

K'' is the imaginary part of the index of refraction of sea water

τ_i is the optical depth with $i = s$ being streak and $i = w$ being white cap

TF is the factor by which foam-free rough surface reflectivity is altered by foam

2.1.4 Model Evaluation

Figures 2-7 and 2-8 demonstrate the application of the surface model in a simple radiative transfer calculation to compute brightness temperature vs. wind speed. The figures are expressed as differential brightness temperatures in degrees above a calm sea ($U = 0.0 \text{ m sec}^{-1}$).

In Figure 2-7 the differential brightness temperatures computed using three foam models are plotted together with two 19.35 Ghz nadir observations. The foam models consist of using the Rosenkranz (1971) attenuation coefficient and: (a) Cardone (1969) white cap coverage; (b) Ross and Cardone (1974) streak coverage with a ratio of streaks to white cap depth of 0.6; and (c) the same with a depth ratio of 0.1. This last model seemed to fit best and was retained.

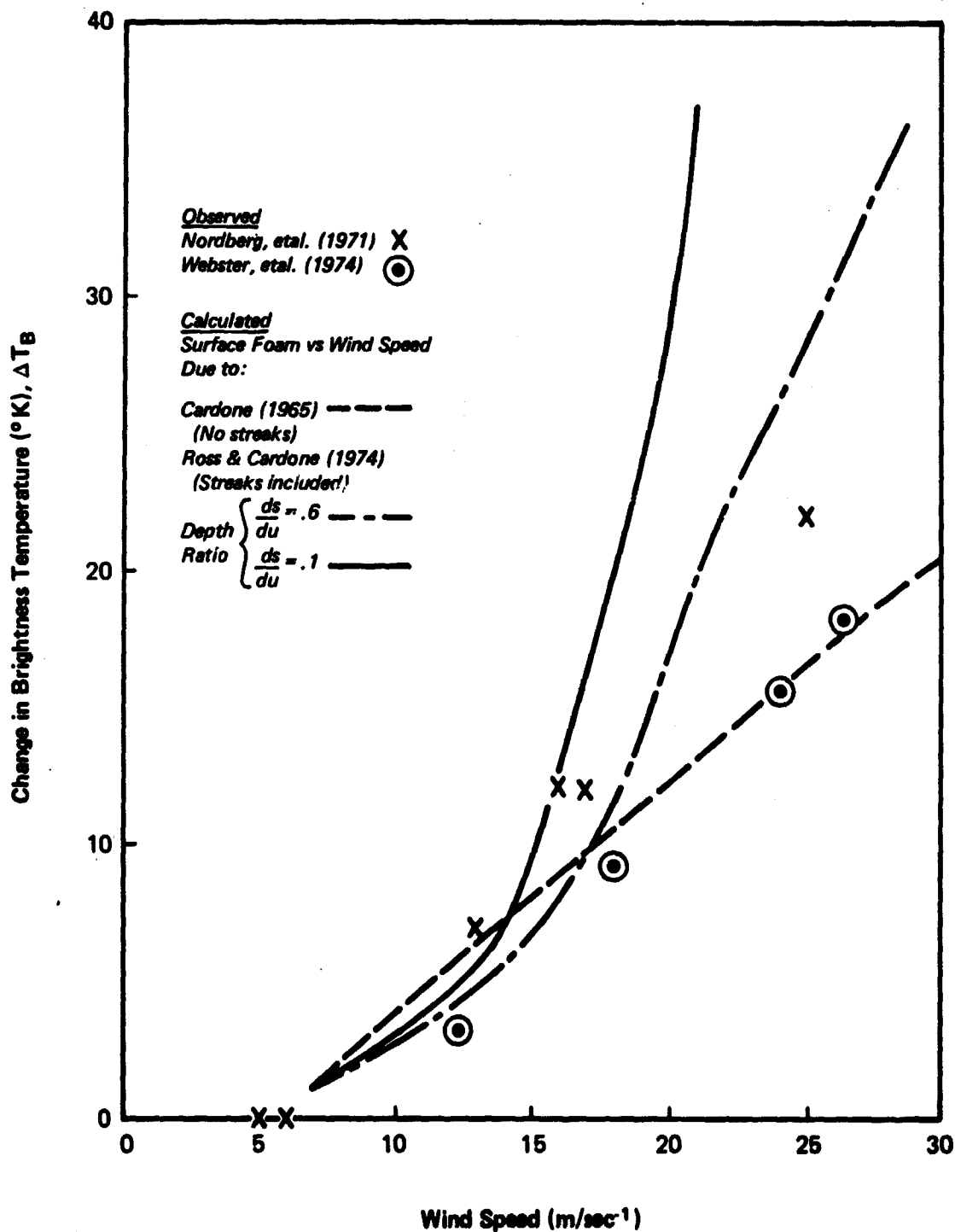


Figure 2-7 Computed Change in Brightness Temperature Using Three Foam Models

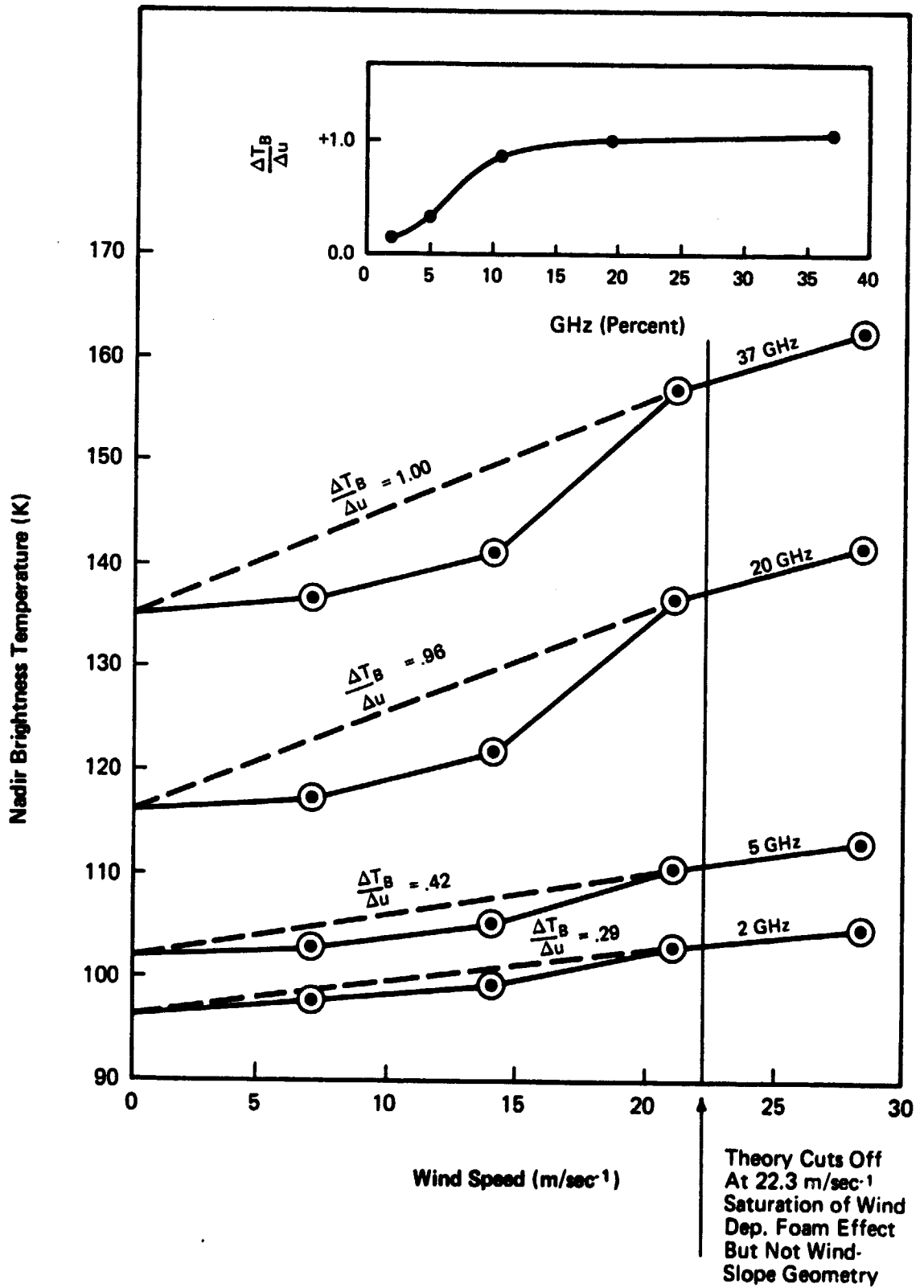


Figure 2-8 Microwave Channel Response to Wind Speed

The brightness temperature dependence on wind speed at three other frequencies (2, 5, and 37 GHz) and temperature wind speed slopes are given in Figure 2-8. The inset plots brightness temperature change versus frequency and essentially demonstrates the frequency dependence of the foam attenuation coefficient.

The model was further evaluated against measurements obtained by BESEX. The details of this experiment are found in Wilheit et al. (1974), and Webster et al. (1974), and in a discussion given in Section 4 of this report. As part of the experiment, the CV-990 aircraft made low level (150 m) measurements at a number of frequencies of brightness temperature over the ice-free Arctic Ocean under various surface wind conditions. These data were used to compare with the model computations.

Since it was reported by Wilheit et al. (1974) that the brightness temperature as measured by the aircraft radiometers suffered apparent linear offsets in the absolute calibration, comparisons were made with the change in brightness temperature with wind speed, that is

$$\frac{\Delta T_B}{\Delta U} (\lambda)$$

Figure 2-9 shows the data reported in Webster et al. (1974) and the model computed values. The agreement is quite good.

2.2 Precipitation Model

2.2.1 Background

An important feature of the simulation and inversion software implemented at GSFC is the ability to generate, through simulation, large statistical samples of brightness temperatures, at any given set of frequencies, for different ensembles of geophysical parameters using sets of physical and radiometric models which require very little computation time to execute. One important radiometric model defines the effects of precipitation on microwave radiation. As part of this program, an investigation was performed to arrive at a first model which would satisfy the need for computation economy without sacrificing unduly the physics of the problem. The model adopted and modified is

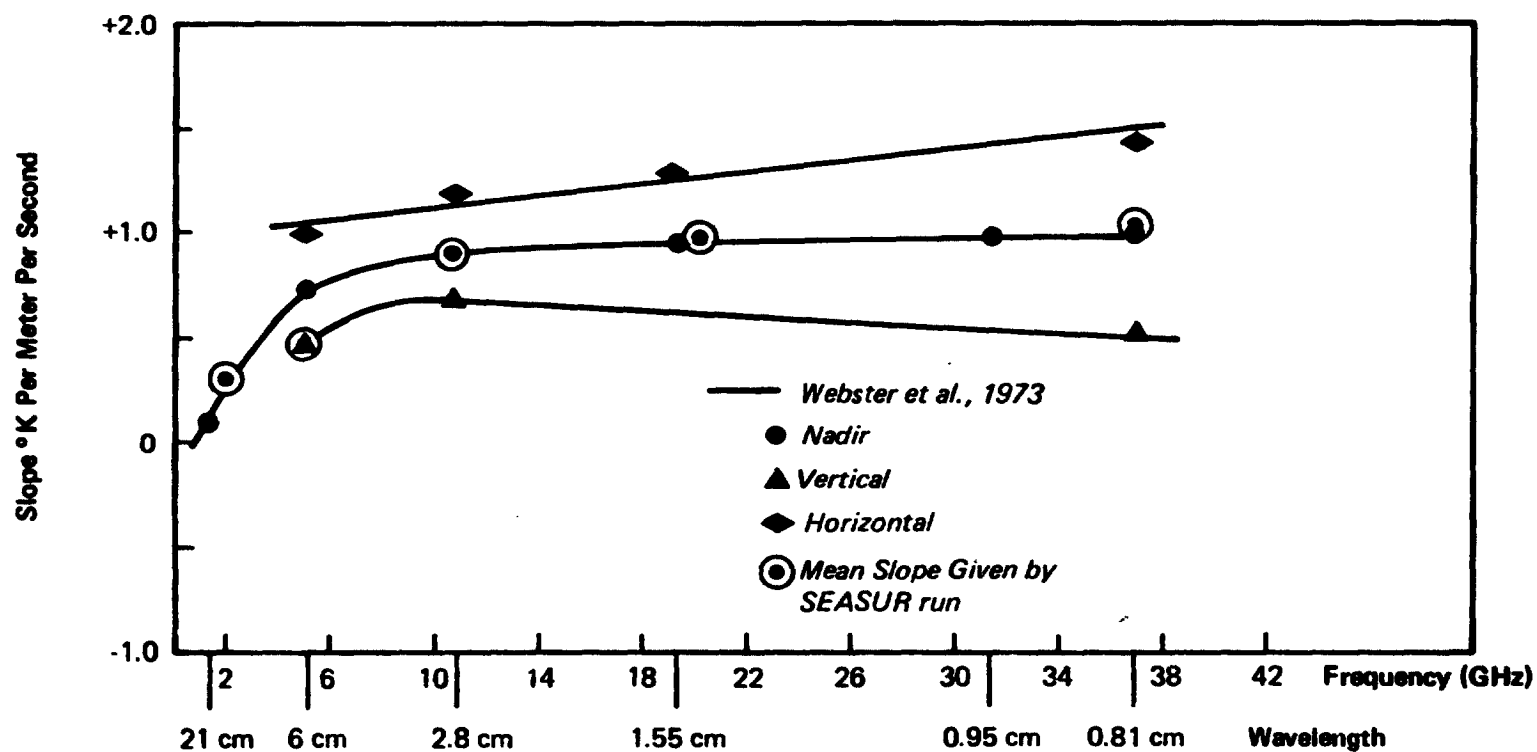


Figure 2-9 Comparison of Change in Brightness Temperature Due to Increases with Wind Speed

one previously described by Gaut et al. (1975). A more accurate model designed for the treatment of varying cloud raindrop distributions has since been developed (Fowler et al., 1976).

2.2.2 Theoretical Considerations of the Extinction Model

The starting point for the model development is the unit volume extinction coefficient which, for precipitation with a spectrum of drop sizes $N(r)$, is given by:

$$\gamma_E \left[\bar{n}(\lambda, T), r \right] = \int_0^{\infty} N(r) Q_E \left[\bar{n}(\lambda, T), r \right] r^2 dr \quad (2-12)$$

where

γ_E is unit volume extinction coefficient (neper m^{-1})

$N(r)$ is drop size distribution function ($cm^{-3} \mu m^{-1}$)

Q_E is the Mie efficiency factor for extinction

$\bar{n}(\lambda, T)$ is the complex index of refraction (dimensionless)

λ is wavelength (cm)

r is drop radius (μm)

and T is absolute temperature ($^{\circ}K$)

Furthermore, according to Mie (1908)

$$Q_E = \frac{2}{q} \sum_{\ell=1}^{\infty} (2\ell + 1) \operatorname{Re} \left(a_{\ell}(\bar{n}(\lambda, T), q) + b_{\ell}(\bar{n}(\lambda, T), q) \right) \quad (2-13)$$

where a_{ℓ} and b_{ℓ} are the well-known coefficients in the Mie series, and $q = [2\pi r / (\lambda \times 10^4)]$ is the dimensionless drop size parameter. The complex index of refraction of water at centimeter wavelengths is given by the Debye Formula (1929):

$$\bar{n}^2 = \frac{\epsilon_0 - \epsilon_{\infty}}{1 + i(\lambda_0/\lambda)} + \epsilon_{\infty} \quad (2-14)$$

Here ϵ_0 and ϵ_∞ are the static and optical dielectric constants and λ_0 is the Debye relaxation wavelength.

Since the complex index of refraction, \tilde{n} , is a function of temperature and wavelength, $Q_E(\tilde{n}, \lambda, r)$ must be specified for each λ and T , as well as for each r . Due to the series summation in Expression 2-13, this is not an easy matter computationally.

2.2.3 Approximations of the Extinction Model

An alternate form for the Mie extinction efficiency factor is given by a power series expansion in the dimensionless drop size parameter.

$$Q_E(\lambda, r, T) = qZ(\lambda, T) + q^3 A(\lambda, T) + q^4 B(\lambda, T) + \dots \quad (2-15)$$

where

$$\begin{aligned} Z &= 4 \operatorname{Im} \{-K\} = 4 \operatorname{Im} \left(-\frac{\tilde{n}^2 - 1}{\tilde{n}^2 + 2} \right) \\ A &= -\frac{4}{5} \operatorname{Im} \left(\frac{\tilde{n}^2 - 1}{\tilde{n}^2 + 2} \frac{\tilde{n}^4 + 27\tilde{n}^2 + 38}{2\tilde{n}^2 + 3} \right) \\ B &= 8/3 \operatorname{Re} \left(\frac{\tilde{n}^2 - 1}{\tilde{n}^2 + 2} \right) \end{aligned}$$

This expansion is valid for all values of q .

The Staelin Approximation

When $q \ll 1$, that is, when $\lambda \ll r$, Equation 2-15 reduces to:

$$Q_E \rightarrow qZ(\lambda, T) \quad \text{for} \quad q \rightarrow 0$$

This approximation basically defines the Rayleigh limit appropriate to the scattering of microwaves by cloud droplets.

Substituting into Expression 2-12,

$$\gamma_E = \int_0^\infty N(r) qZ(\lambda, T) \pi r^2 dr = mF(\lambda, T) \quad (2-16)$$

where

$$m = \frac{4\pi\rho}{3} \int_0^{\infty} N(r) r^3 dr$$

is the mass density of the
droplet ensemble

and

$F(\lambda, T)$ is a function of wavelength and temperature only. This function has been evaluated empirically by Staelin (1966) for which the expression becomes:

$$\gamma_E = \frac{1.0016 \times 10^4 m}{\lambda^2} 10^{0.0122(291-T)} \quad (\text{neper m}^{-1}). \quad (2-17)$$

This says that the unit volume extinction of a nonprecipitating cloud is proportional to its mass density (m) regardless of the nature of the droplet distribution. This is not true, however, for a precipitating cloud and this approach is not applicable.

Large Drop Approximation

Figure 2-10 shows a computation of Q_E as a function of q . It is seen that as $q \rightarrow \infty$, $Q_E \rightarrow 2$ (Geometric Limit). Therefore, for large droplets which have $r \gg \lambda$, Q_E can be approximated by 2.

ERT-Approximation - First Model

An average raindrop has a characteristic radius on the order of $10^3 \mu\text{m}$. At a wavelength of 1 cm, the q parameter is of order 1. The Rayleigh limit is no longer valid and, furthermore, it must be recognized that the extinction factor will vary orders of magnitude within the size range of the rainfall droplets. For complete accuracy, the full Mie Theory using Equation 2-13 should be used in this range of drop sizes. This would be feasible if all raindrops had the same radius and atmospheric temperature structure was isothermal. However, distributions of droplet radius and atmospheric vertical temperature structure make a layered computation using Equation 2-13 computationally complex.

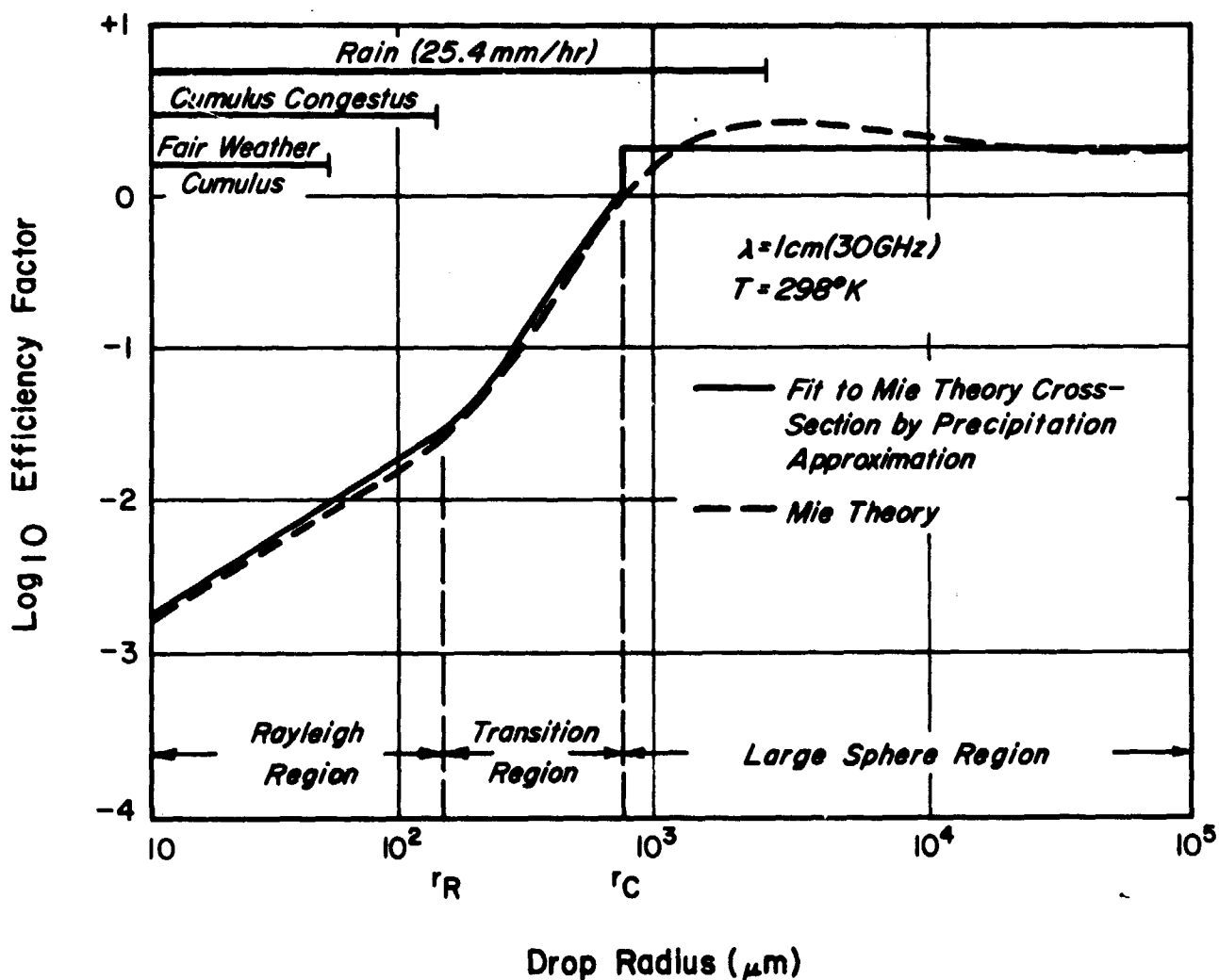


Figure 2-10 Range of Drop Sizes and Mie Efficiency Factors for Full Mie Theory and Linear Segment Approximation

The approach taken here was to assume that the Mie expression (Equation 2-15) could be approximated by a small number of terms. Also, the number of terms included was assumed to be dependent on the size range of the droplets such that the attenuation coefficient can be expressed as:

$$\begin{aligned} \gamma_E &= \int_0^{\infty} N(r) Q_E(r, \lambda, T) \pi r^2 dr \\ &\approx \int_0^{r_1} N(r) Q_E(r_1) \pi r^2 dr + \int_{r_1}^{r_2} N(r) Q_E(r_2) \pi r^2 dr \\ &\quad + \dots \dots \int_{r_n}^{\infty} N(r) Q_E(r_n) \pi r^2 dr \end{aligned} \quad (2-18)$$

for $n + 1$ size intervals. Ideally, each of the above integrals should be expressible in closed form.

Three size intervals or regions are assumed, each with its own approximation to the Mie efficiency factor as follows:

$$\begin{aligned} Q_E &= qZ && \text{for } 0 \leq r \leq r_R \\ &= qZ + Aq^3 + Bq^4 && \text{for } r_R \leq r \leq r_C \\ &= 2 && \text{for } r \geq r_C \end{aligned} \quad (2-19)$$

The quantities q , Z , A , and B are as previously defined.

The limits r_C and r_R are specified in the following manner. The upper limit to the Rayleigh region is taken where the dimensionless drop size parameter reaches 0.10. This is approximately the point at which the q^3 term in Equation 2-15 reaches 10% of the leading term in q .

Thus,

$$q_R = 0.10$$

and

$$r_R = (1.59 \times 10^2) \lambda.$$

The lower limit of the large sphere region is located by specifying the position of the optical resonance region. The general criteria adopted is:

$$r_c = \frac{\lambda \times 10^4}{2|\bar{n}|}$$

where

$$|\bar{n}| > \pi$$

With these approximations, Equation 2-18 becomes:

$$\begin{aligned} \gamma \approx & \int_0^{r_R} qZN(r) \pi r^2 dr + \int_{r_R}^{r_c} (Aq^3 + Bq^4) N(r) \pi r^2 dr \\ & + \int_{r_c}^{\infty} 2 N(r) \pi r^2 dr \end{aligned} \quad (2-20)$$

2.2.4 The Precipitation Drop Size Model

In order to Evaluate Equation 2-20 in closed form, the drop size distribution must be specified. The particular form of the drop size distribution $N(r)$ is empirically determined and for the purpose of our study, the most general specification for cloud droplet spectra is the Deirmendjian (1964) distribution:

$$N(r) = Ar^{C_1} \exp \{-Br^{C_2}\} \quad (2-21)$$

which characterizes the ensemble in terms of four parameters, two of which (A and B) are scale parameters, the others being shape parameters. Fair weather and stratus clouds conform nicely to this characterization. A simple form of the Deirmendjian distribution may be used to describe precipitation.

A review of the literature, especially that pertaining to radar studies of precipitation, indicated that the Marshall-Palmer (1948) model of drop size distribution for precipitation is the most appropriate for studies of satellite-measured brightness temperatures. The

virtues of this model are that: (1) an empirical expression exists which relates the drop size distribution (useful in computations of radiative interaction) to the instantaneous rainfall rate (useful in synoptic studies), and (2) the form of the expression is essentially that of the Deirmendjian expression used in modeling cloud droplet distributions.

The Marshall-Palmer model is expressed as:

$$N(r,R) = k_1 \exp - \{k_2 r R^{-k_3}\} \quad (2-22)$$

where

$$k_1 = 16.0 \times 10^{-6}$$

$$k_2 = 8.156 \times 10^{-3}$$

$$k_3 = 0.21$$

and

$N(r,R)$ is the number density of particles per unit size range ($\text{cm}^{-3} \mu\text{m}^{-1}$)

r is the droplet radius (μm) for a given rain rate

R is the rainfall rate (mm/hr)

This is essentially the Deirmendjian distribution with parameters:

$$A = k_1$$

$$B = k_2 R^{-k_3}$$

$$C_1 = 0$$

$$C_2 = 1$$

2.2.5 The Combined Model

Substituting Equation 2-22 into Equation 2-20 and evaluating, the extinction coefficient becomes a function of wavelength, temperature, and rainfall rate:

$$\gamma(\lambda, T, R) = \sum_{n=1}^7 C_n F_n(\lambda) G_n(\lambda, T) H_n(\lambda, R) R^{0.21n} \quad (2-23)$$

where

C_N are constants

and

F_N, G_N, H_N are functions of the indicated variables.

3. INVERSION PROCEDURE OPTIMIZATION

3.1 Summary of the Inversion Procedure

The inversion-simulation procedure implemented at GSFC has been described in previous reports such as Gaut et al. (1972) and Willand et al. (1974). This procedure is shown schematically in Figure 3-1. Briefly, the approach uses physical and interaction models operating on an ensemble of atmospheric data (including clouds and precipitation) to create a correlation matrix or "D-Matrix" between brightness temperatures at selected frequencies and geophysical parameters of interest. This D-Matrix is then used to "infer" from actual radiometric measurements the values of the corresponding geophysical parameters.

In the normal procedure, the correlation matrix (and the D-Matrix) include a priori statistics most representative of the annual climatic condition appropriate to the region of interest. As a consequence, the ensemble would include both cloudy (and precipitating) and clear sky conditions, calm and rough seas, and varying profiles of atmospheric temperature and water vapor, with the statistical distribution of these conditions determined by climatology. An acceptable argument can be made that with this kind of "mixed" D-Matrix, the inversion results, on a seasonal basis, must be optimized in a statistical sense. However, for any given situation, especially when the general condition (clear, cloud; calm, rough) can be independently determined, a D-Matrix can be constructed, again based on a priori data, which would be more representative of the actual situation. Given this specially tailored D-Matrix, it is argued that better inversion results can be obtained.

Tests were performed to evaluate the improvement in inversion results using specially tailored D-Matrices. The analysis addressed only the two simple situations: clear and cloudy conditions. A decision scheme, based on differences between two channels, was used to differentiate between clear and cloudy skies. This decision scheme was also tested. Results are presented in this section.

Another aspect of the inversion procedure investigated was the way in which the correlation matrix is formed. Normally, the matrix consists of only linear terms. The question was raised, and addressed, as to the effect of including nonlinear terms in the correlation.

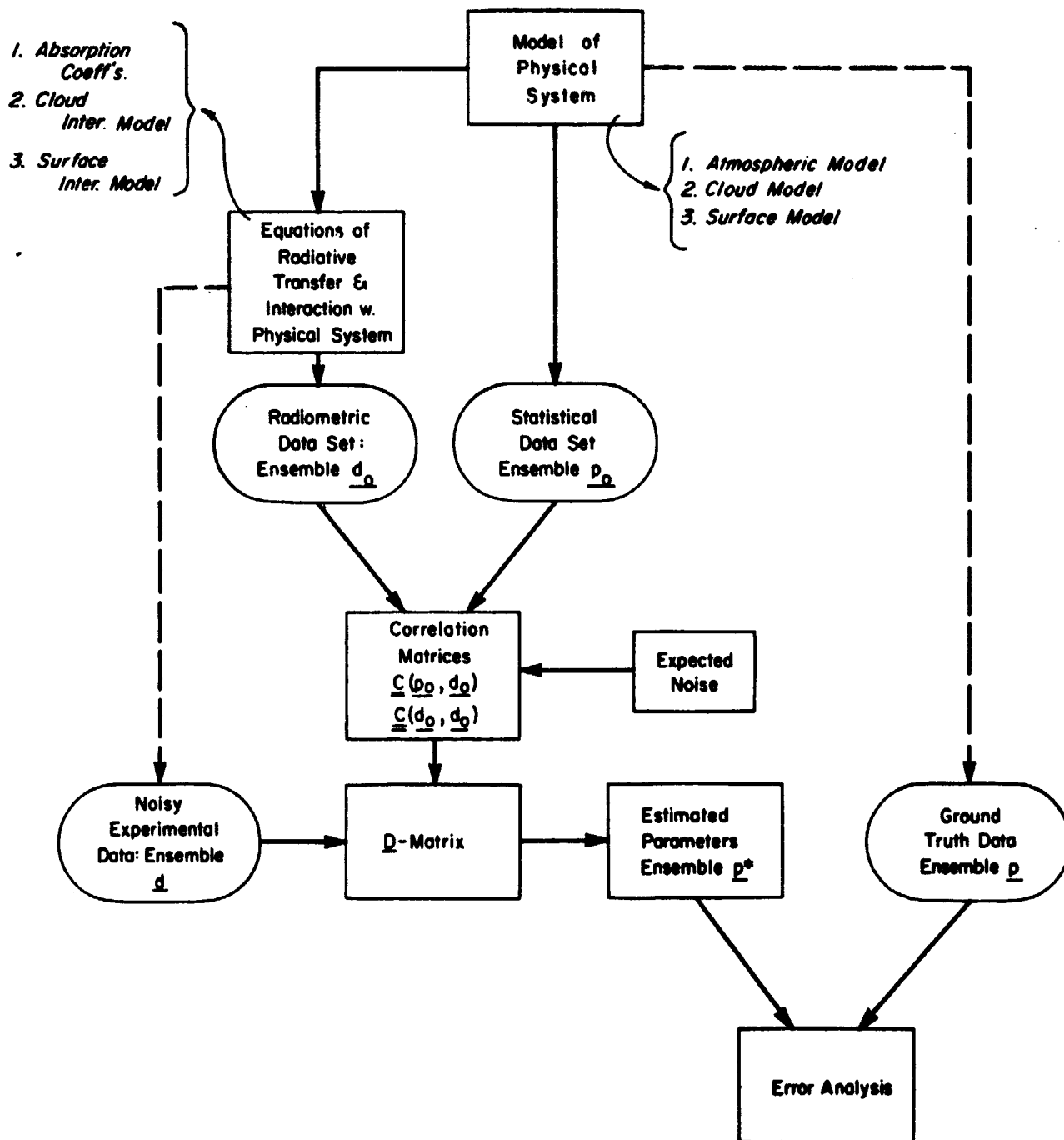


Figure 3-1 Flow Diagram for Application of the Data Inversion Methodology to Parameter Estimation for a Radiometric Experiment

3.2 D-Matrix Selection

A simple experiment was conducted to test the effects of D-Matrix selection on inversion results. In this experiment, two different D-Matrices were generated, each from an ensemble of 60 sets of geophysical data. The first D-Matrix was generated using data sets which contained clouds (and/or precipitation). The second D-Matrix was generated using only data with clear sky conditions. The parameters and channel frequencies used are shown in Table 3-1.

These two D-Matrices were applied to two ensembles of simulated brightness temperatures generated from a different set of geophysical conditions. Again, the first data set included only cloudy conditions, while the second was generated from clear sky data only.

The inversion results from this experiment are shown in Table 3-2. The important data in this table are the Figures of Merit, which is defined as the improvement of the inversion results (in a statistical sense) over that obtained from "guess" based on climatology. The Figures of Merit show that when a D-Matrix is used with the appropriate data set (clear sky D-Matrix with clear sky data, cloudy D-Matrix with cloudy data), the inversion results, in a statistical sense, are quite good (that is, Figure of Merit > 1.5). These results do not seem to degrade appreciably in the case when a cloudy D-Matrix is applied to clear sky conditions. However, in the case in which a clear sky D-Matrix is applied to cloudy data, the degradation in the inversion results is dramatic, with Figures of Merit < 1 indicating results which are worse than a climatological guess.

Analysis was performed to arrive at a clear/cloudy condition discrimination such that an operational procedure for D-Matrix switching can be implemented. The choice of this discrimination was limited to the channels identified in Table 3-1. The analyses included single and multiple-channel approaches. The final selection made is given below:

$$\begin{aligned} [T_B(31.4 \text{ GHz}) - T_B(19.35 \text{ GHz})] &< 20.5^\circ\text{K} \quad \text{clear} \\ &\geq 20.5^\circ\text{K} \quad \text{cloudy} \end{aligned}$$

TABLE 3-1
MICROWAVE CHANNELS AND GEOPHYSICAL PARAMETERS
USED IN THE INVERSION ANALYSIS

Channel Number		Channel		
		Freq. GHz	Angle	Pole
1	1	1.42	0°	H
2	2	4.99	38°	V
3	3	10.69	38°	V
4	4	10.69	38°	H
5	5	19.35	0°	H
6	6	22.235	0°	V
7	7	31.4	0°	V
8	8	37.0	38°	V
9	9	37.0	38°	H

Parameter Number		Parameter	Units
10	1	Sea Surface Temperature	°K
11	2	Wind Speed	m sec ⁻¹
12	3	Integrated Water Vapor (W.V.)	g cm ⁻²
13	4	Integrated Liquid Water	g cm ⁻²
14	5	Mode Radius	μm
15	6	W.V. 0-500m	g m ⁻³
16	7	W.V. 500-1500m	g m ⁻³
17	8	W.V. 1500-3500 m	g m ⁻³
18	9	W.V. 3500-11000m	g m ⁻³

TABLE 3-2

INVERSION RESULTS -- 60 OBSERVATIONS FOR D AND 60 OBSERVATIONS (ALL ARCTIC) FOR EVALUATION

INDEX	PARAMETER VALUE		STD.DEV.	INVERSION ERRORS		FIGURE OF MERIT	INDEX	PARAMETER VALUE		STD.DEV.	INVERSION ERRORS		FIGURE OF MERIT		
	MEAN	STD.DEV.		PERCENT	MEAN			PERCENT	MEAN		STD.DEV.	PERCENT		MEAN	PERCENT
1	273.6433	1.1726	4.0-73	1.48	-5.0192	-1.83	0.290	1	273.6433	1.1726	0.9077	0.33	-0.1013	-0.04	1.292
2	8.6352	4.2915	13.0000	147.92	15.9527	180.56	0.320	2	8.6352	4.2915	3.2227	36.48	0.1519	1.72	1.332
3	1.0000	0.3576	0.7500	65.04	0.7576	71.01	0.405	3	1.0000	0.3576	0.0770	7.22	0.0220	2.14	4.044
4	0.0310	0.0204	0.0204	65.84	-0.0310	-100.00	1.000	4	0.0310	0.0204	0.0048	31.48	0.0033	10.64	2.042
5	-44.4991	40.8658	40.8658	91.84	-44.4991	-100.00	1.000	5	-44.4991	40.8658	27.3313	61.42	0.7808	1.77	1.495
6	4.0965	1.1147	2.4437	59.65	2.9703	72.51	0.456	6	4.0965	1.1147	0.7549	17.94	-0.0445	-1.09	1.517
7	3.1579	1.0332	2.2792	72.17	2.6294	83.26	0.453	7	3.1579	1.0332	0.5570	17.64	0.1002	3.17	1.855
8	1.9764	0.7049	1.2341	62.38	0.9689	48.97	0.571	8	1.9764	0.7049	0.2272	11.49	-0.0079	-0.40	3.102
9	0.2008	0.1404	0.2173	109.23	0.2032	101.19	0.646	9	0.2008	0.1404	0.0757	37.66	0.0221	11.01	1.850

CLEAR D AND CLOUDY DATACLOUDY D AND CLOUDY DATA

INDEX	PARAMETER VALUE		STD.DEV.	INVERSION ERRORS		FIGURE OF MERIT	INDEX	PARAMETER VALUE		STD.DEV.	INVERSION ERRORS		FIGURE OF MERIT		
	MEAN	STD.DEV.		PERCENT	MEAN			PERCENT	MEAN		STD.DEV.	PERCENT		MEAN	PERCENT
1	273.6433	1.1726	0.0374	0.23	-0.0774	-0.03	1.840	1	273.6433	1.1726	0.9177	0.34	-0.3669	-0.14	1.278
2	8.6352	4.2915	2.0648	30.16	0.1444	1.63	1.610	2	8.6352	4.2915	3.2036	36.32	-0.6111	-5.72	1.534
3	0.5367	0.2702	0.0363	7.14	0.0029	0.54	7.049	3	0.5367	0.2702	0.0668	12.62	0.0030	0.50	3.926
4	0.0	0.0	0.0	100.00	0.0	100.00	0.0	4	0.0	0.0	0.0020	100.00	0.0007	100.00	0.0
5	0.0	0.0	0.0	100.00	0.0	100.00	0.0	5	0.0	0.0	4.5355	100.00	18.0631	100.00	0.0
6	2.9582	0.9301	0.4532	15.32	-0.0937	-3.17	2.052	6	2.9582	0.9301	0.5096	17.23	-0.3632	-12.98	1.825
7	1.8741	0.6523	0.3734	20.03	-0.0655	-3.49	2.270	7	1.8741	0.6523	0.4142	22.15	-0.2562	-15.76	2.000
8	0.7243	0.5098	0.2064	28.49	0.0073	1.01	2.858	8	0.7243	0.5098	0.1730	23.89	0.1304	19.10	3.000
9	0.1753	0.0691	0.0520	69.08	0.0171	22.67	1.328	9	0.1753	0.0691	0.0576	70.47	0.0275	30.68	1.200

CLEAR D AND CLEAR DATACLOUDY D AND CLEAR DATA

The rationale for selecting this threshold condition is given in Figure 3-2 in which simulated values of $[T_B(31.4 \text{ GHz}) - T_B(19.35 \text{ GHz})]$ are plotted against cloud liquid water content. The data indicate minimum effects due to varying surface roughness (or windspeed), and have a defined intercept of $\sim 20^\circ$ to 21°K for liquid water content approaching zero. This technique was tested in the cases to be discussed in Section 4 and showed that accurate decisions were made in all situations.

3.3 Nonlinearities

The D-Matrix, as employed in the statistical regression algorithm for estimating the geophysical properties of the ocean surface and the intervening atmospheric conditions, has as its formulation:

$$\underline{D} = \underline{C}(\underline{P}, \underline{d}) \cdot \underline{C}^{-1}(\underline{d}, \underline{d}) \quad (3-1)$$

where \underline{d} is the prediction data vector, and \underline{P} is the predicted parameter vector. This formulation does not consider any nonlinear relationships between \underline{d} and \underline{P} . The quality of the estimated parameters can be degraded by the existence of nonlinear relationships if they are not treated properly. Any nonlinearities must be treated in the formulation of the D-Matrices in order for them to be considered in making parameter estimates.

The existence and impact of nonlinear relationships were investigated by providing for the incorporation of nonlinear terms in the generation of the D-Matrices. A data basis function vector $\underline{\phi}(\underline{d})$ was defined such that $\underline{\phi}(\underline{d})$ could be composed of linear and squared terms of \underline{d} . For example, $\underline{\phi}$ might contain the following representations of \underline{d} :

$$\begin{aligned} \phi_1 &= d_2 \\ \phi_2 &= d_3 \\ \phi_3 &= d_4 \\ \phi_4 &= d_5 \\ \phi_6 &= d_1^2 \end{aligned}$$

The D-Matrix is now defined by:

$$\underline{D} = \underline{C}(\underline{P}, \underline{\phi}) \cdot \underline{C}^{-1}(\underline{\phi}, \underline{\phi}) \quad (3-2)$$

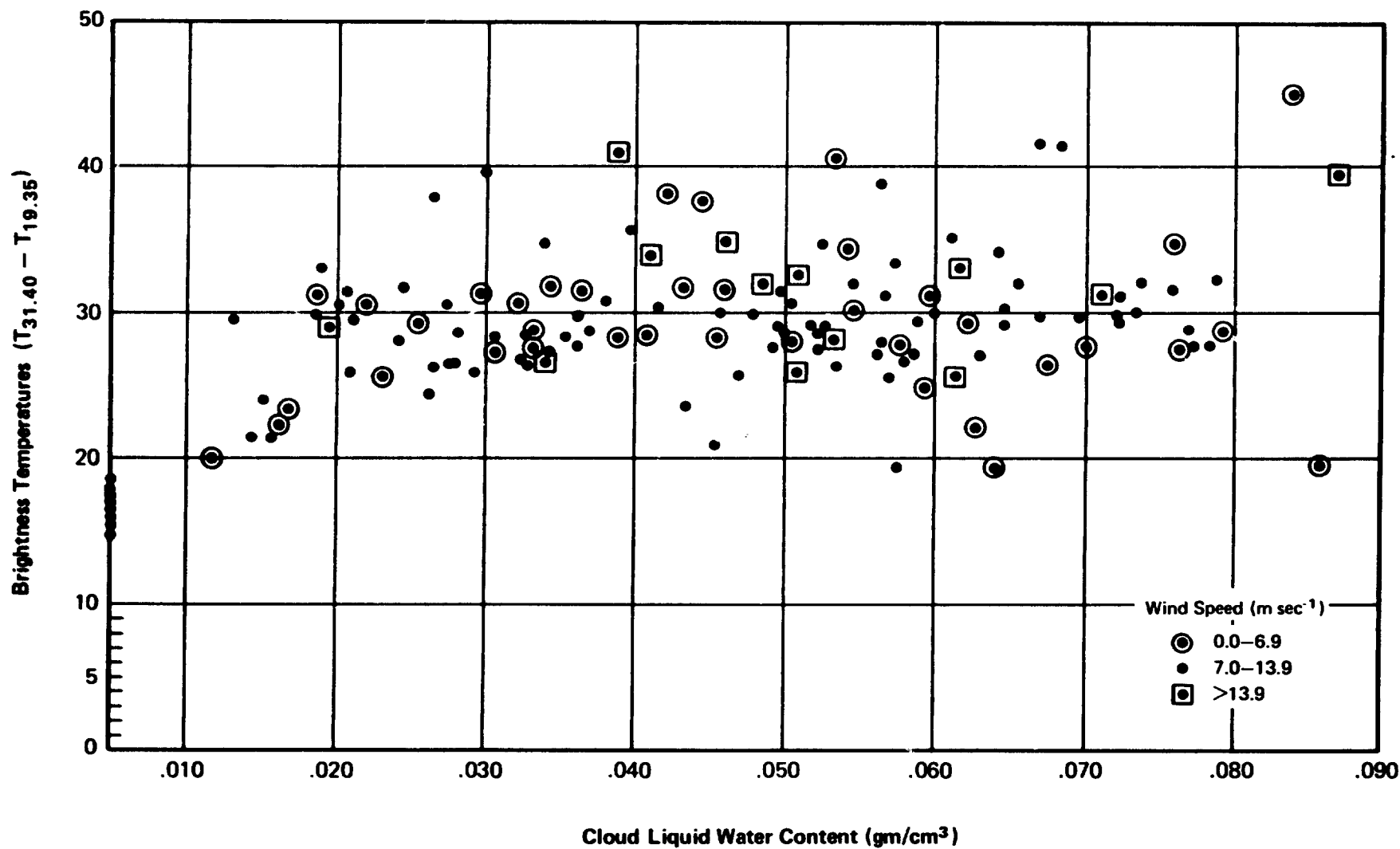


Figure 3-2 Brightness Temperature Differences vs Cloud Liquid Water Content:

This provides the capability to investigate the correlation of nonlinear representations for any prediction data vector and the results obtained for inferences with the data basis function so defined.

Also, a parameter basis function vector $\underline{\theta}(P)$ was defined such that $\underline{\theta}(P)$ could be composed of linear or nonlinear representations of P . Several nonlinear representations are included for use at the programmer's option.

The D-Matrix, defined by the new data basis function vector and the new parameter basis function vector, is:

$$\underline{D} = \underline{C}(\underline{\theta}, \underline{\phi}) \cdot \underline{C}^{-1}(\underline{\phi}, \underline{\phi}) \quad (3-3)$$

The capability now provided allows for the expression of any or all terms of $\underline{\theta}$ and $\underline{\phi}$ as linear or nonlinear terms. If all linear terms are chosen, the definition of the D-Matrix is once again that of Equation (3-1). In general, no significant differences in retrieval results were obtained for inversions employing nonlinear representations for either the data basis functions or the parameter basis functions. However, no attempt was made in this study to define which nonlinear representations are most valid in describing data-parameter relationships. Incorporation of nonlinearities (such as, an exponential response of brightness temperature to liquid water) should produce improved inversion results.

3.4 Channel-Parameter Correlations

Correlation coefficients between channel brightness temperatures and geophysical parameters are now provided as part of the improved inversion system. These correlations are of interest in themselves, and are also useful as the basis for optimizing (that is, minimizing) the channel configuration for any given set of geophysical parameters. While no actual optimization analysis was performed during the course of this study, the correlation coefficients were analyzed to understand better the contributory effects of each of the channels to the acquisition of the various parameters.

Figures 3-3 through 3-5 show the correlation coefficients between the set of channels identified in Table 3-1 and the parameters of sea surface temperature, surface wind speed, integrated water vapor, and

integrated liquid water content. The correlations with sea surface temperature (Figure 3-3) are generally low for all frequencies with the maximum values found in the surface channel at 4.99 GHz. Physically this is realistic, for the very low frequency channels are most sensitive to salinity, and wind effects become strong beyond 6 GHz. Furthermore, the strongest physical dependence of microwave radiation on sea surface temperature occurs at the frequency of 6 GHz. The correlations for the cloudy case appear higher than those for the clear, but this is due merely to artificial (random) correlations and is not statistically significant. In fact, the only correlation which is clearly statistically significant for a sample this size is the correlation between 4.99 GHz and the surface temperature.

The high correlation between surface wind speed and brightness temperature under clear conditions (Figure 3-4) explains much of the low correlation with the surface temperature. As shown in the previous section, wind speed effects cause large changes in the emissivity of the ocean surface, and thus cause far greater changes in surface brightness temperatures than occur due to variations in surface temperature. Thus, channels which are highly dependent on surface emission show a much stronger dependence on wind speed than on temperature. The maximum sensitivity to this parameter, under clear conditions, occurs at 10.69 GHz with correlations dropping to 0.6 only for the surface channel (4.99 GHz) and the water vapor channel (22.235 GHz).

The sensitivity of the channels to wind speed changes significantly when cloudiness occurs, resulting in decreasing correlation with increasing frequency, and indicating that the 1.42 GHz channel is the most useful for inferring wind speeds. Figure 3-5, showing the high correlation of frequencies greater than 10 GHz with liquid water, explains this loss of sensitivity. It also shows the strong correlation of frequencies near 22.235 GHz with water vapor when no clouds are present and the reduction in sensitivity to water vapor when liquid water is also found.

In data sets of this size, correlations greater than 0.2 are statistically significant at the 95-percent level, indicating that channels with higher correlations should provide data for inversion of that parameter. Thus, sea surface temperature can be inferred from channels at 1.42 and 4.99 GHz under all atmospheric conditions, although

the lack of a really strong correlation might impair the results somewhat. All channels provide data on wind speed under clear conditions, while frequencies lower than 11 GHz provide good information when clouds are present. Water vapor is best inferred from channels between 22.235 and 31.4 GHz with channels at 19.35 and 37 GHz also aiding inversions under clear conditions. For inversion of liquid water contents, the frequencies of 31.4 and 37 GHz are the most useful, while frequencies between 10.69 and 22.235 GHz should also provide excellent data.

The effects of these correlation coefficients on inversion results can be seen more clearly in the elements of the D-Matrix. Tables 3-3 and 3-4 show the D-Matrices computed using, respectively, clear sky and cloudy data. As can be seen from the D-Matrix elements, the 1.42 and the 4.99 GHz channels are dominant in the inversion for sea surface temperature, although other channels contribute because of the very small variation in correlation with frequency. The wind speed coefficients are also easily interpreted in light of the correlations, for the 10.69 GHz channels and the channels greater than 30 GHz are the key data sources for the winds under clear conditions. When clouds are present, the 1.42 and the 10.69 GHz channels become dominant.

The dependence of water vapor and liquid water on individual channels is small when clouds are present. Under clear conditions, the D-Matrix relies upon the 22.235 GHz channel to define the water vapor content, but this channel alone ceases to be sufficient when liquid water is sensed. Little frequency dependence is seen in the correlation with water vapor for frequencies between 1.42 and 19.35 GHz and for frequencies between 22.235 and 37 GHz, and the difference between these two frequency ranges is quite small. Likewise, there is little sensitivity to frequency in the liquid water correlations when the frequency exceeds 10 GHz. Thus, for cloudy conditions, the D-Matrix relies on the correlations between the atmospheric parameters and all the selected frequencies to separate and infer liquid water and water vapor. In a channel optimization approach, however, fewer of these channels could be used, since it is apparent that many of the frequencies supply similar, possibly redundant information. In fact, inversion results might be improved through more careful channel selection.

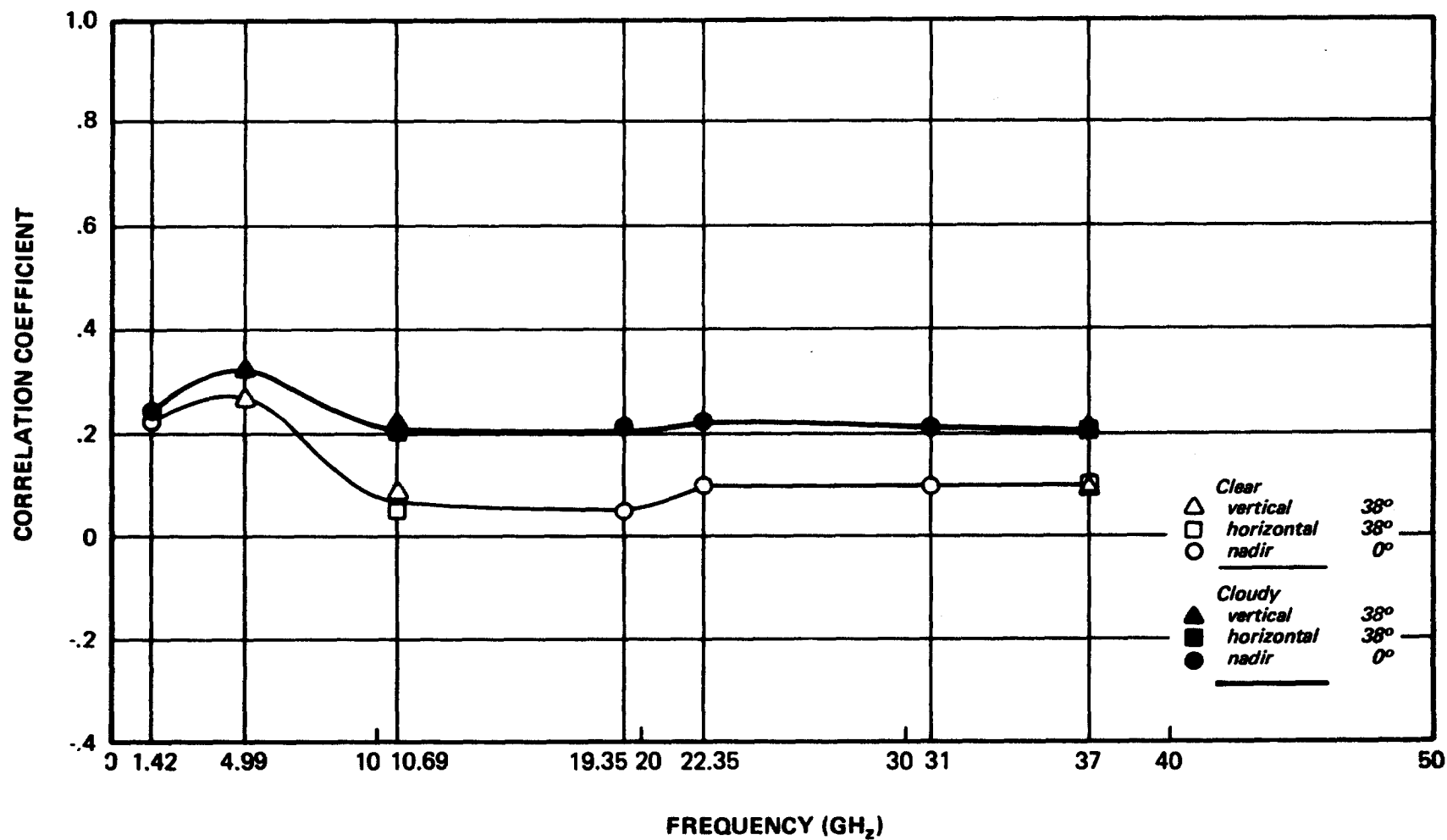


Figure 3-3 Correlation Coefficients Between Microwave Measurements and Sea Surface Temperature

40

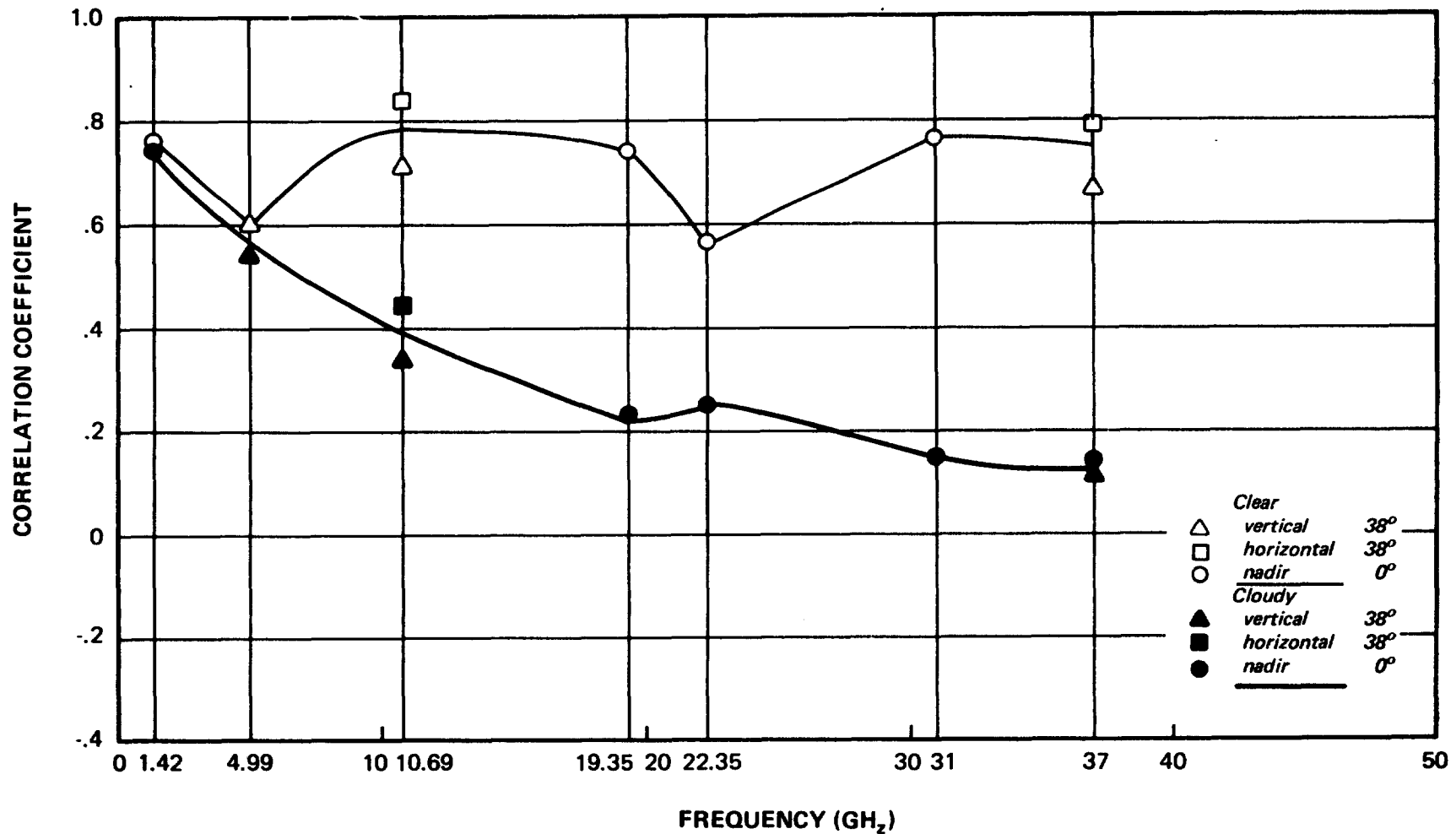


Figure 3-4 Correlation Coefficients Between Microwave Measurements and Surface Wind Speed

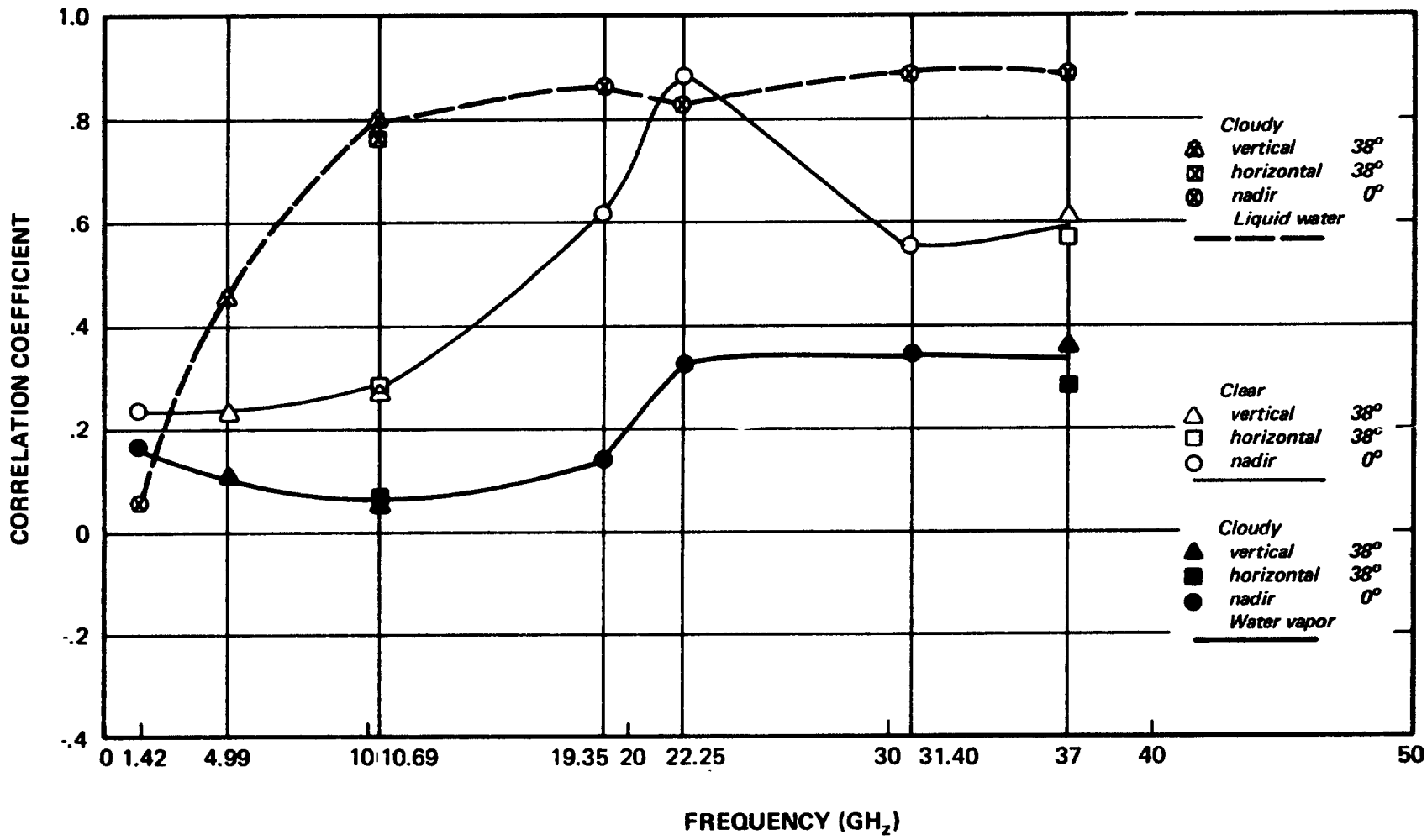


Figure 3-5 Correlation Coefficients Between Microwave Measurements and Atmospheric Water Vapor and Liquid Water

TABLE 3-3

CLEAR -- NO NOISE -- D-MATRIX

D-MATRIX FOR ORIGINAL DATA BASIS FUNCTIONS
THE FIRST 6 STATISTICALLY ORTHOGONAL BASIS FUNCTIONS WERE USED

2.7351E 02	1.2933E 02	2.2125E 02	-5.9631E 01	-4.6274E 00	-9.2070E 01	3.9639E 01	-1.3919E 02	-5.9628E 01	1.2315E 02
9.3375E 00	7.7646E 01	1.8233E 01	-2.1373E 02	1.8688E 02	-8.9087E 01	2.3531E 01	-1.0877E 02	-1.8055E 02	2.0520E 02
5.6442E-01	2.3219E 00	3.5385E 00	-3.8019E 00	-4.0351E 00	-1.2500E 00	8.2535E 00	-2.9928E 00	-7.9000E-01	3.9390E 00
0.0	0.0	0.0	0.0	0.0	0.0	0.0	0.0	0.0	0.0
0.0	0.0	0.0	0.0	0.0	0.0	0.0	0.0	0.0	0.0
3.0106E 00	1.4658E 01	2.3059E 01	-2.3137E 01	-2.5752E 01	-1.3201E 01	1.4213E 01	-1.1756E 01	8.9165E 00	4.7308E 01
1.9185E 00	7.7936E 00	1.4158E 01	-1.3626E 01	-2.3194E 01	-6.4049E 00	1.4879E 01	-5.5450E 00	9.5878E 00	2.9013E 01
7.7717E-01	2.0412E 00	2.3113E 00	-4.5779E 00	-3.3224E 00	2.5652E-01	1.9033E 01	-4.9831E 00	-5.3500E 00	-2.6199E 00
8.8812E-02	5.3521E-01	6.7655E-01	-4.8913E-01	3.1524E-01	-9.3213E-04	3.0110E 00	-1.1384E 00	-1.4994E 00	-1.0718E 00

42

TABLE 3-4

CLOUDY -- NO NOISE -- D-MATRIX

D-MATRIX FOR ORIGINAL DATA BASIS FUNCTIONS
THE FIRST 8 STATISTICALLY ORTHOGONAL BASIS FUNCTIONS WERE USED

2.7351E 02	1.1267E 02	9.0201E 01	-8.6562E 01	-1.7881E 01	4.7283E 01	-1.7513E 01	5.5122E 01	2.1285E 01	-4.8933E 01
9.3375E 00	2.7114E 02	-3.3414E 01	-4.5359E 02	2.7547E 02	1.4373E 01	9.5330E-01	-2.4315E 01	-3.3702E 01	3.1675E 01
1.0628E 00	1.1930E 01	1.9521E 00	-1.2576E 01	2.0602E-01	8.0949E 00	9.7903E 00	-1.8104E 01	1.5450E 01	-2.9175E 00
7.3577E-02	-1.9374E 03	-7.3515E-01	2.0233E 00	-2.1145E-01	-1.1079E 00	4.3354E-01	-1.8980E-01	-7.2642E-01	7.6587E-01
4.0644E 01	5.5843E 03	1.5608E 03	-5.9027E 03	3.1143E 02	4.3529E 03	-1.3073E 03	3.9567E 02	3.1314E 03	-2.4367E 03
4.1186E 00	6.4147E 01	-7.0144E 00	-6.4300E 01	8.4319E 00	7.5205E 01	6.2293E 00	-9.6942E 01	1.0626E 02	-2.6003E 01
3.2143E 00	7.5570E 01	2.6239E 00	-7.7923E 01	7.1578E 00	7.4563E 01	6.9561E 00	-8.2015E 01	9.9554E 01	-2.9183E 01
1.9197E 01	3.6781E 01	8.1914E 00	-3.9723E 01	1.1357E 00	2.4552E 01	1.1583E 01	-3.1030E 01	3.4711E 01	-1.1130E 01
2.1006E-01	-8.2537E 00	5.3637E-01	8.5167E 00	-1.5464E 00	-1.0709E 01	7.8213E 00	1.5341E 00	-8.8808E 00	4.6756E 00

4. INVERSION OF BESEX DATA

4.1 The BESEX Experiment

The Bering Sea Expedition (BESEX) was a joint US-USSR scientific study to obtain detailed information on the atmospheric and geophysical characteristics of the Bering Sea area. A large portion of the international waters was designated as the test area; within this area the NASA Convair 990, a Russian IL-8, the American icebreaker STATEN ISLAND, and the Russian weather ship PRIBOI all made extensive measurements during February and March 1973. One phase of the study investigated the response of microwave sensors to clouds with varying liquid water content. Another aspect of the experiment attempted to determine the response of various microwave frequencies to differences in sea state, sea ice and sea surface temperature; the ships were used to make concurrent observations of the appropriate surface parameters. The complement of microwave radiometers (down looking) on board the aircraft is that identified previously in Table 3-1. A more detailed description of the experiment is given by Wilheit et al. (1974). This experiment provides good data to test the new models and inversion algorithms. For this purpose, one set of data, that for 3 March 1973, was selected for detailed analysis.

4.2 Meteorological Conditions for 3 March 1973

The experiment performed on 2 and 3 March 1973 sampled an extensive cloud system associated with a dissipating warm occlusion and a developing secondary cyclone (Figure 4-1). The measurements were made at altitudes of 0.16, 2, 4 and 11 km along a narrow strip from 55°W, 171°W (point A, Figure 4-1) to 58.3°, 172.5°W (point B, Figure 4-1), a flight path almost perpendicular to the primary frontal system and intersecting the secondary low centered at 55°N and 170°W.

On the day prior to this flight, the primary low had been located near 49°N, 173°E with the associated frontal system trailing to the southeast and beginning to occlude. This cyclone moved northwestward to 54°N, 170°E during the twenty-four hours previous to the flight, with no

7432

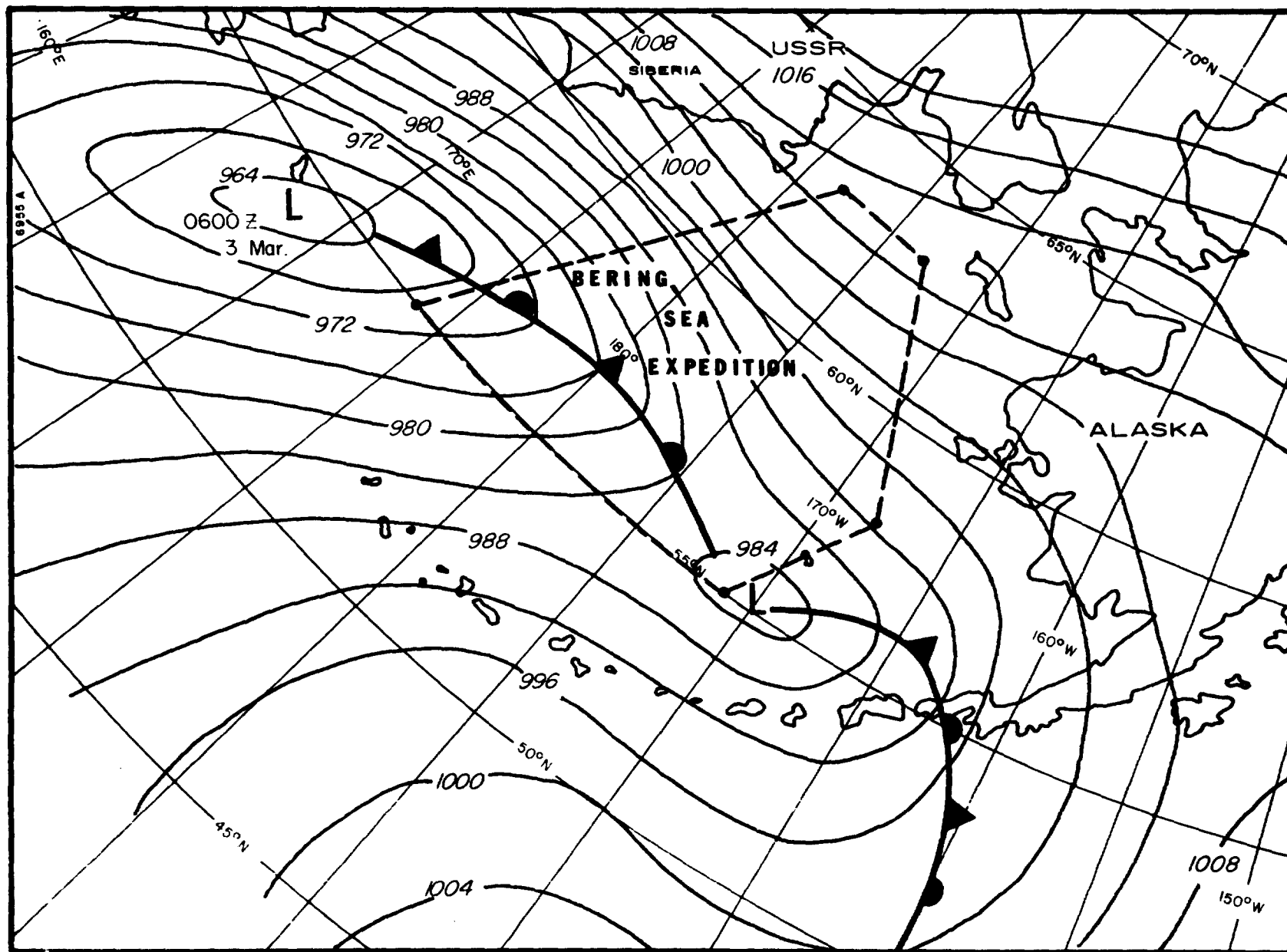


Figure 4-1 Surface Chart for the BESEX Area, 0000 GMT, March 3, 1973

change occurring in the central pressure. At the same time, the frontal system swung well to the northeast into the Bering Sea test area and advected a significant amount of warm air ahead of the system. This warm air mass was forced aloft as the system became occluded. At the time of the experiment (2300 GMT, 2 March 1973 - 0230 GMT, 3 March 1973), the front was thoroughly occluded, and no traces of the warm air mass were found at the surface.

Shortly before 0000 GMT, 3 March 1973, vorticity advection behind the front led to the development of a secondary cyclone near 55°N, 170°W. This cyclone effectively cut off most of the warm air advection associated with the primary front, and began feeding warm, moist air into the surface layer beneath the second cold air mass. The resulting air mass contrasts encountered during the flight are shown in a schematic representation based on that developed by Danielsen (1959) in Figure 4-2. The associated cloud system and the aircraft measurements of wind are shown in a similar format in Figure 4-3. (Since these analyses represented a composite of four hours of measurements during which the system moved 50 km north, the exact position of the front varies with the time of microwave sampling.)

The observations made from the Convair 990 showed that the clouds were structured into a multilayered stratiform system with maximum cloud heights below 10.5 km. North of 57°N, a cirrus canopy topped the system between altitudes of 8 and 10 km with a thin layer of cirrocumulus forming its base at 7.5 km. Below this canopy was a layered mass of altostratus and altocumulus which stretched as far south as 56.5°N and formed the top of the cloud mass throughout most of the warm air sector. Underneath this layer was one of dense altostratus topping at 6 km as far south as 56.6°N, then dropping to 4.5 km as the cloud penetrated the secondary cold front. In the regions where clouds occurred above the altostratus, the layers were frequently separated by a thin strip of clear air.

Below 4 km, the stratiform pattern began to change to a cumuliform situation. Multilayered altocumulus was found between 2 and 4 km from 58°N almost as far south as 55°N; beneath this stratocumulus, cumulus and stratus fractus were found from 2 km down to below 100 m in altitude. These clouds were quite cellular in structure below 200 m, and the cells

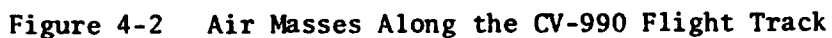




Figure 4-3 Clouds, Temperature and Winds Along the CV-990 Flight Track

often appeared to grow and dissipate during the experiment. The upper cloud levels were far more stable in structure, with differences due more to the slow northward motion of the front than to marked internal changes.

The Convair 990 sampled this cloud system at four different levels, 11 km, 4 km, 2 km and 160 m. The high level pass was above the entire cloud mass, from south to north. Upon its completion at 57.5°N, the aircraft descended through cirrus, cirrostratus and altostratus to 4 km and the sampling of cloud droplets was begun. The 4-km pass was made primarily in the altostratus layer, although the stretch between 56.5°N and 56°N occurred in the clear air strip separating the altostratus from stratocumulus, and only clear air was encountered south of 55.6°N. The cloud particle samples of altostratus made at this level indicated that the cloud was at least partially frozen north of 56.5°N, and primarily liquid south of 56°N (Fowler et al., 1974).

Near 55°N, the aircraft turned and descended to 2 km to begin a northward run through the stratocumulus. This leg of the flight was continuously in cloud and was characterized by very limited variability in the cloud parameters along the flight path. The final pass of the experiment was made through the cloud base at 150 m; this started at 57.5°N and terminated at 55°N. The cloud liquid water content varied considerably at this level. Heavy snow, limited visibility, and easterly winds of 35 to 40 knots were reported north of 56°N. South of this boundary, a change to rain and decreasing winds showed the penetration of the low level warm air mass. This change in air mass was also indicated by the termination of the main cloud system and the occurrence of small cumulus cells.

A small segment, ten minutes of data (230454 to 231512 GMT), from this flight was selected for analysis. The location of this data segment is shown in Figure 4-2 as lying between 55°N and 56.5°N. During this time the aircraft was flying at 11 km (3500 ft) and passed over the location of the surface frontal position (note wind shift). For most of the flight, the aircraft was flying over an undercast of stratocumulus, altocumulus and altostratus layers. The winds, extrapolated to the surface, were estimated to be of the order of 30 to 35 kts (approximately 15 m sec^{-1}). Since no ice was encountered along this flight

segment, and since the flight path was near the edge of the pack ice, the sea surface temperature is estimated to be of the order of $273 \pm 1^\circ\text{K}$, a value which agrees well with infrared surface measurements made on clear days during the BESEX Experiment.

4.3 Microwave Measurements

The brightness temperatures measured by the downward-looking radiometers for this flight segment are shown in Figure 4-4. The data shown include correction for the viewing geometry as illustrated in Figure 4-5. However, no calibration correction has been applied to the data. It has been pointed out in Wilheit et al. (1974) that the data have systematic offsets. A procedure was developed, based on comparison between simulated and measured values, to arrive at an objective set of brightness temperatures for the full complement of channels.

The offsets were arrived at as follows: a set of 100 environmental profiles (including clouds and surface properties) were generated using data corresponding to the climatological regime of the BESEX area and cloud models applicable to the frontal system shown in Figure 4-3. These profiles were used to simulate the corresponding set of 100 brightness temperatures for each of the channels. The means of the simulated data were compared with the averaged value of the measured data with the differences adopted as the channel offsets. These offsets, the system noise values, and the sample means and standard deviation, are shown in Table 4-1. It is interesting to note that with very few exceptions the standard deviations are less than 10% of the corresponding mean values, and that the only extreme offset is found for the 4.99 V channel, a channel which was malfunctioning (personal communication, Wilheit, 1975).

4.4 Inversion Results

The selected segment of microwave measurements was inverted using the models and techniques described in previous sections. The a priori data consisted of February and March soundings from St. Paul's Island

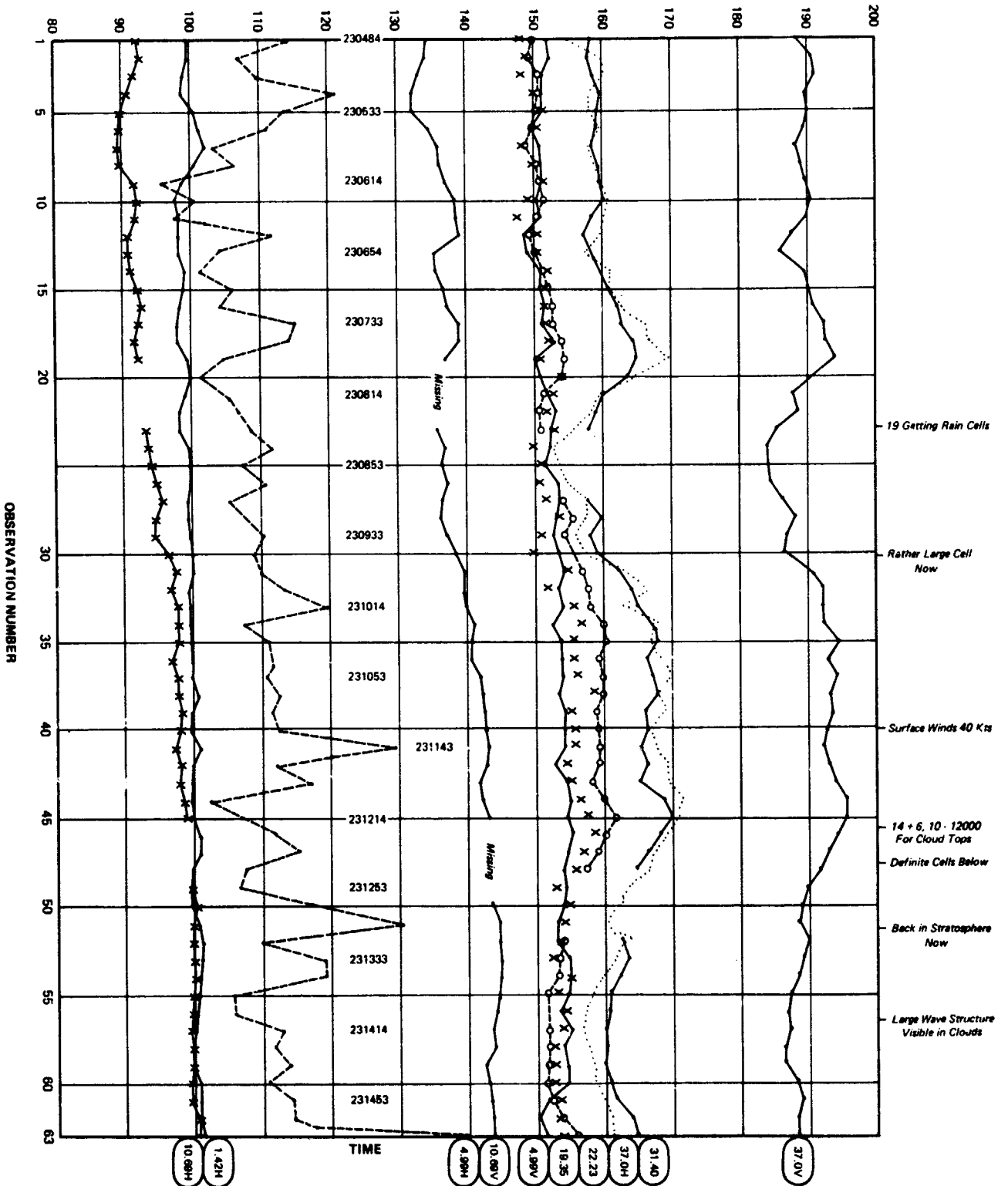
BRIGHTNESS TEMPERATURES ($^{\circ}$ K) "Before Offsets"

Figure 4-4 Microwave Measurements from 11 Km, 3 March 1973

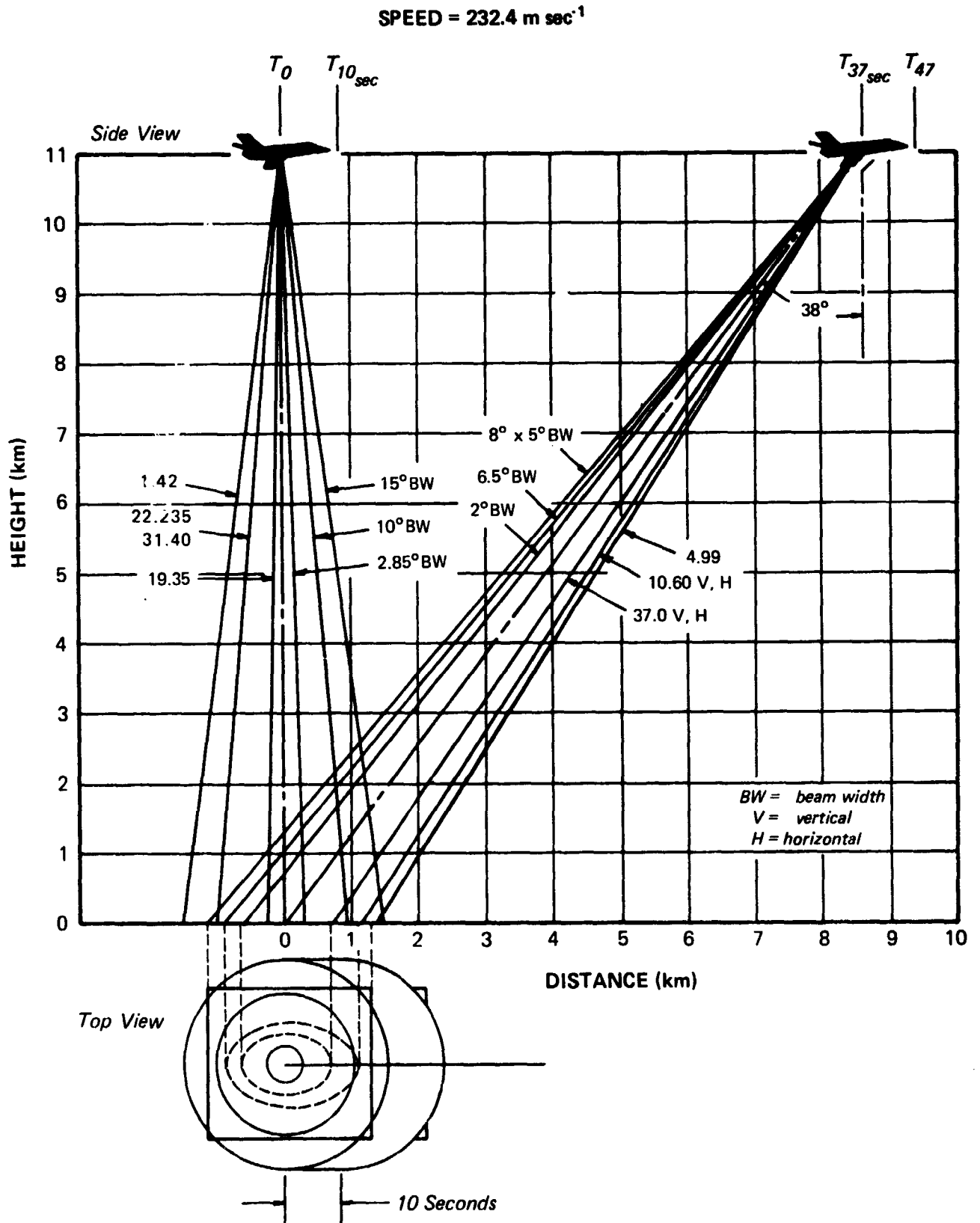


Figure 4-5 Multi Channel Microwave Field of View from 11 Km

TABLE 4-1
MICROWAVE RADIOMETER OFFSETS AND SYSTEM NOISE

No.	Channel	Theoretical		Actual Data		(a-b)	System Noise
		Average (°K)	σ (°K)	Average (°K)	σ (°K)	Offset (°K)	
1	1.42 H	99.66	0.63	99.58	.91	-5.9	1.0
2	4.99 V	120.02	1.69	152.7	1.62	-32.7	3.8
3	10.69 V	132.50	4.41	139.5	3.28	-7.0	0.8
4	10.69 H	98.64	6.05	95.57	3.49	3.1	0.8
5	19.35 H	138.59	9.57	152.71	2.5	-14.1	1.0
6	22.235 V	155.59	11.57	153.9	3.63	1.7	1.6
7	31.4 V	165.66	15.44	102.06	3.42	3.6	1.0
8	37.0 V	199.87	15.35	189.76	3.85	10.1	3.8
9	37.0 H	173.44	21.68	161.76	4.82	11.7	1.1

(57°N, 170.2°W) collected from 1957 to 1963 while cloud models were derived from cloud particle samples made during the flight on 3 March 1973. The sea surface parameters were randomly selected from wind statistics compiled from the St. Paul's Island data, and from the Bering Sea temperature statistics measured during the Bering Sea Experiment. Two sets of atmospheric models were derived from the a priori data, one set representing only clear conditions and the other, only cloudy conditions.

Simulation of the brightness temperatures corresponding to these models used the new sea surface roughness and precipitation models. Noise was randomly added to the completed radiometric measurements to simulate the system noise shown in Table 4-1. The atmospheric models and simulated brightness temperatures were then correlated and "clear" and "cloudy" D-Matrices were generated. No nonlinearities were incorporated in the D-Matrix generation but the use of clear and cloudy D-Matrices permitted a test of the D-Matrix switching approach discussed in Section 3.2.

Figure 4-6 shows the parameters of sea surface temperature, surface wind speed, integrated liquid water and integrated water vapor content inferred from the measured microwave data. In all samples the measured atmospheric conditions were cloudy and the inversion procedure accurately selected the cloudy D-Matrix for use. Agreement of the inverted parameters with the meteorological conditions seen in Figures 4-2 and 4-3 is quite good, although the sea surface temperature results do appear to be slightly high and more variable than would be expected. This is due primarily to the malfunctioning of the 4.99 GHz channel, identified by the correlation analysis as providing the optimum information on sea surface temperature. Thus the data set lacked a strong sea surface temperature channel (see Section 3.4). However, the divergence of the values from the a priori mean of 273.5°K demonstrates that the D-Matrix is responding to the measured data despite the absence of strong channel-parameters correlations.

On the other hand, the inverted wind speed values are excellent due to the strong correlation of the 10.69 GHz channels with this parameter. The decrease in wind speed which occurred with the wind

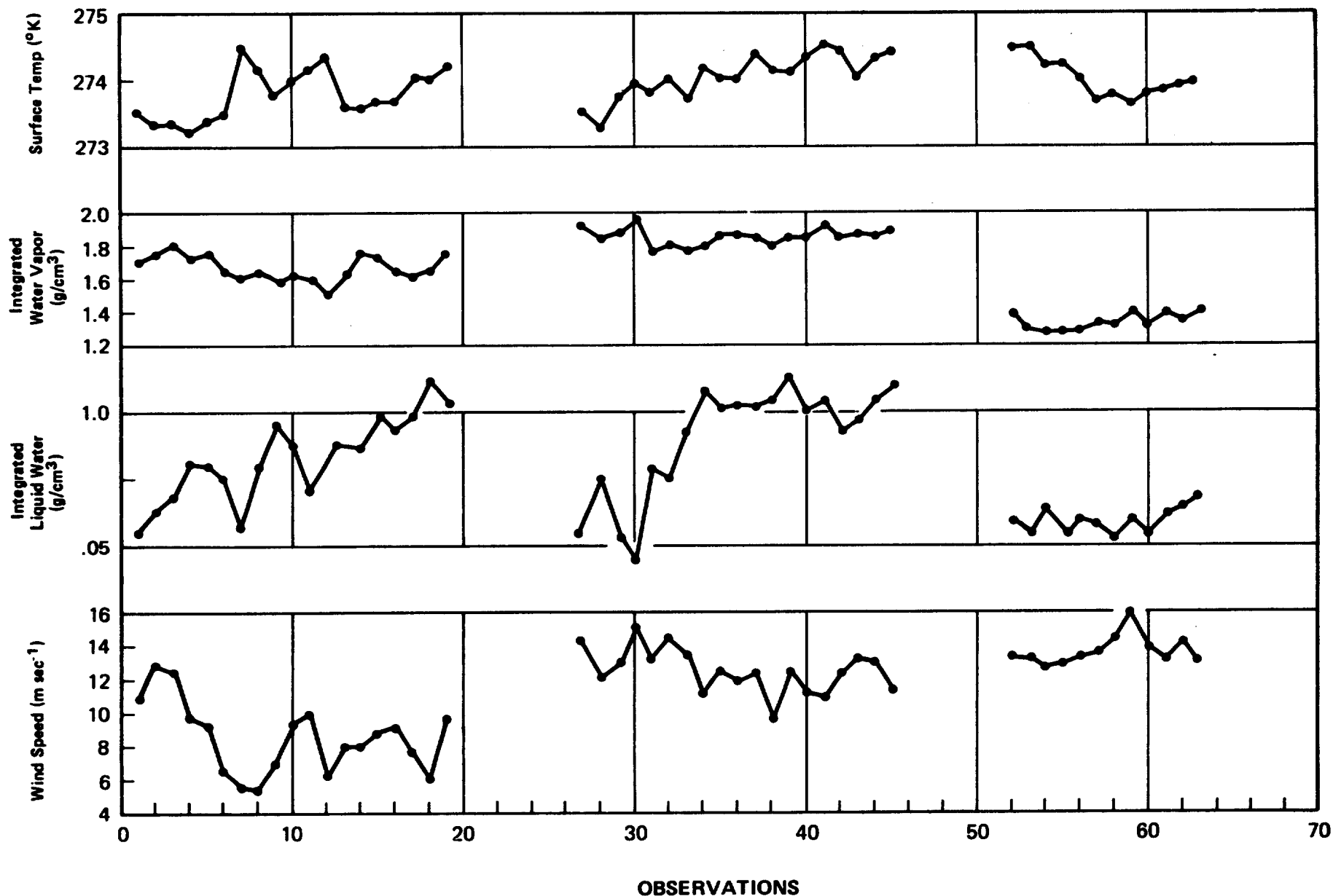


Figure 4-6 Inversion Results from the Measurements Made in the 11 Km Data Set Run (See Figure 4-4)

direction shift at the front is clearly delineated at the proper location. (Because of system movement north during the experiment, the schematic shown in Figure 4-3 shows the front at 56°N , its location at the end of the mission. At 2300 GMT it was nearer 55.5°N .) Wind speeds north of the front are generally 12 to 15 m sec^{-1} corresponding well to the winds of 12 to 17 m sec^{-1} deduced from aircraft measurements. The increase in wind speed south of the frontal zone is also indicated by the first few points.

The inversions for integrated water vapor and integrated liquid water content show very reasonable values. For these parameters, it was difficult to determine precise values from the available aircraft data although Wilheit et al. (1974) estimates water vapor contents of 1.3 to 1.8 m^{-3} and liquid water contents of 0.015 to 0.05 g m^{-3} for this time segment. However, both the liquid water and water vapor values do show their maximum in the frontal zone, which was the region of maximum convective activity. They also clearly indicate the decrease in total moisture content and the absence of liquid precipitation associated with the cold surface air north of the front. In general the water vapor contents change little within each of the three air masses indicated, but do show the air masses boundaries in agreement with meteorological observations. The liquid water values are higher than would be expected, but do respond sharply to the small, variable convective cells imbedded in the surface layer, and thus the variability in liquid water provides another means of identifying the frontal zone and identifying the decreases with increasing stability north of the front.

The inversion of this selected data segment demonstrates several factors. First, the relative utility of the selected channel package in inferring the four parameters discussed above agrees with the correlation analysis presented in Section 3. The best results are obtained for surface wind speed, with good results also found for integrated water vapor and liquid water. More difficulty is encountered in the determination of sea surface temperature, due to the absence of a channel strongly correlated with that parameter. For all parameters the inferred results departed significantly from the a priori mean and corresponded well to the trends seen in the measured brightness temperatures (Figure 4-4).

Even more encouraging, the parameter values reliably reflect the meteorological conditions which they represent. Finally, the inversion results demonstrate the reliability of the new models and techniques, with the value of the new sea state model most clearly identified.

5. CONCLUSIONS AND RECOMMENDATIONS

During this study, a new sea state roughness model has been developed which incorporates recent microwave measurements better to define the relationship between surface wind speed and radiometric brightness temperatures. This model takes into account the differences in emissivity between white caps and foam streaks and shows good agreement with empirically derived values. A precipitation model has also been included in the microwave simulation package to extend the cloud model to incorporate the effects of large drops. The approach taken avoided the computational difficulties of a full scattering treatment by expressing the Mie extinction efficiency factors as a power series and approximating that series by a small number of terms. These terms were then used with Marshall-Palmer drop size distribution to derive an expression for the extinction coefficient as a function of rainfall rate.

The inversion procedure was also modified to permit the incorporation on nonlinear parameter-data relationships and to allow D-Matrix switching, using information provided by microwave measurements. This option allows the selection of the D-Matrix most appropriate to data inversion (such as, clear/cloudy sky, land/sea background) by comparison of brightness temperature differences found between channels appropriate to the selection criteria. In an analysis of the value of this option in switching between clear and cloudy D-Matrices, inversion results were seen to be improved over those derived through use of a mixed clear/cloudy D-Matrix. The inversion package was further modified to permit the output of the inter-correlations between parameters and data. This change greatly facilitates the interpretation of the relationship between microwave measurements and geophysical values and the optimization of channels for inversion.

Inversion of microwave data measured during the Bering Sea Experiment demonstrated the reliability of the above models and inversion procedures. It also demonstrated the value of the microwave system carried by the NASA Convair 990 aircraft in measuring meteorological parameters such as surface wind speed and atmospheric water vapor and liquid water content and in defining many of the characteristics of a frontal system.

It is recommended that further study be done on the type of nonlinearities which best express parameter-data relationships and improve inversion results. It is also recommended that the correlations now available be used to select the optional subset of microwave channels for inversion of the desired parameters and that the value of this approach be demonstrated through the use of both simulated and measured data. Finally, it is recommended that surface models representative of land and sea-ice conditions now under development be incorporated into the simulation package to permit an analysis of the usefulness of microwave sensors in inferring a number of surface parameters such as soil moisture or surface vegetation coverage.

6. REFERENCES

- Cardone, V. J., 1969: Specification of the Wind Field Distribution in the Marine Boundary Layer for Wave Forecasting, Report TR69-Y, Geophysical Science Laboratory, New York Univ.
- Danielson, E. F., 1959: The laminar structure of the atmosphere and its relation to the concept of a tropopause, Archiv Fur Geophysik und Meteorologie, Klimatologie A, 3.
- Debye, P., 1929: Polar Molecules, Dover Press.
- Deirmendjian, D., 1964: Scattering and polarization properties of water clouds and hazes in the visible and infrared, Applied Optics, 3, 2, 187.
- Fowler, M. G. J. H. Willand, D. T. Chang and T. L. Cogan, 1974: Studies in the Use of Cloud Type Statistics in Mission Simulation, Final Report, Contract NAS5-28721, Environmental Research & Technology, Inc., Concord, MA.
- Fowler, M. G., K. R. Hardy, and N. D. Sze, 1976: The Development of a Model to Infer Precipitation from Microwave Measurements, Final Report, Contract No. NAS5-20868, Environmental Research & Technology, Inc., Concord, MA.
- Gaut, N. E., M. G. Fowler, R. G. Isaacs, D. T. Chang and E. C. Reifenstein, III, 1975: Studies of Microwave Remote Sensing of Atmospheric Parameters, Final Report, Contract F19628-73-C-0195, Environmental Research & Technology, Inc., Concord, MA.
- Gaut, N. E., E. C. Reifenstein, III and D. T. Chang, 1972: Microwave Properties of the Atmosphere, Clouds and the Oceans, Final Report. Contract NAS5-21194, Environmental Research & Technology, Inc.
- Marshall, J. S. and W. M. Palmer, 1948: The distribution of raindrops with size, J. Meteor., Vol. 5.
- Mie, G., 1908: Ann. Phys., Vol. 25.
- Nordberg, W., J. Conway, D. B. Ross and T. T. Wilheit, 1971: Measurements of microwave emission from a foam-covered wind-driven sea, Journal of the Atmospheric Sciences, 28.
- Rosenkranz, P. W., 1971: Radiometric Sensing of Atmospheric Water and Temperature, PhD Thesis, Dept. of Electrical Engineering, M.I.T.
- Rosenkranz, P. W. and D. H. Staelin, 1972: Microwave emissivity of ocean foam and its effect on nadir radiometric measurements, Journal of Geophysical Research, 77.
- Ross, D. B. and V. Cardone, 1974: Observations of oceanic whitecaps and their relation to remote measurements of surface wind speed, Journal of Geophysical Research, 79.

- Staelin, D. H., 1966: Measurements and interpretations of the microwave spectrum of the terrestrial atmosphere near 1-centimeter wavelength, J. Geophysical Research, 71, 1, 2875.
- Stogryn, A., 1967: The apparent temperature of the sea at microwave frequencies, IEEE Transactions on Antennas and Propagation, AP-15(2), 278.
- Webster, W. J., T. T. Wilheit, D. B. Ross and P. Gloersen, 1974: Analysis of the Convair-990 Passive Microwave Observations of the Sea States During the Bering Sea Experiment, Results of the U.S. Contribution to the Joint U.S./U.S.S.R. Bering Sea Experiment, X-910-74-141, NASA Goddard Space Flight Center.
- Wilheit, T. T., M. G. Fowler, G. Stambach and G. Gloersen, 1974: Microwave Radiometric Determination of Atmospheric Parameters During the Bering Sea Experiment, Results of the U.S. Contribution to the Joint U.S./U.S.S.R. Bering Sea Experiment, X-910-74-141, NASA Goddard Space Flight Center.
- Willand, J. H., M. G. Fowler, E. C. Reifenstein, III, and D. T. Chang, 1973: Analysis of Aircraft Microwave Measurements of the Ocean Surface, Final Report, Contract NAS5-21828, Environmental Research & Technology, Inc., Concord, MA.